






Planetary Period Oscillations of Saturn's Dayside Equatorial Ionospheric Electron Density Observed on Cassini's Proximal Passes

G. Provan¹ , S. W. H. Cowley¹ , E. J. Bunce¹, S. E. Milan¹ , A. M. Persoon² , and D. A. Gurnett² 

¹Department of Physics and Astronomy, University of Leicester, Leicester, UK, ²Department of Physics and Astronomy, University of Iowa, Iowa City, IA, USA

Key Points:

- Saturn's equatorial ionospheric electron density data from Cassini's proximal orbits are examined for planetary period oscillations (PPOs)
- Northern and weaker southern PPO modulations occur in the diffusive layer and transport region (~2,500–10,000 km) but not at lower altitudes
- Density maxima occur near the rotating principal meridians for both PPO systems, $\Psi_{NS} \approx 0^\circ$, with typical max/min ratios in the range ~2–10

Correspondence to:

G. Provan,
gp31@le.ac.uk

Citation:

Provan, G., Cowley, S. W. H., Bunce, E. J., Milan, S. E., Persoon, A. M., & Gurnett, D. A. (2021). Planetary period oscillations of Saturn's dayside equatorial ionospheric electron density observed on Cassini's proximal passes. *Journal of Geophysical Research: Space Physics*, 126, e2021JA029332. <https://doi.org/10.1029/2021JA029332>

Received 10 MAR 2021

Accepted 5 AUG 2021

Abstract We examine electron density data obtained in Saturn's dayside equatorial ionosphere during Cassini's proximal periapsis passes, specifically data derived from wave spectra, for evidence of modulation with the planetary period oscillations (PPOs) observed ubiquitously throughout Saturn's magnetosphere. Clear evidence is found on northern hemisphere inbound passes where northern system modulations occur in the ionospheric diffusive layer peaking at a factor of ~7 at ~3,200 km altitude, extending at lesser factors to ~7,000 km altitude in the transport region. Simultaneous southern system modulations by factors ~1.5–2.5 are also found above ~3,400 km. Factor of ~4–10 northern system modulations are also detected in the diffusive layer and transport regions to ~6,000 km in the outbound pass data, though southern system modulations were not clearly discerned within the data scatter. Modulations were not detected in the photochemical equilibrium layer at altitudes ~1,600–2,200 km. Where clear modulations were observed, their phases in the diffusive layer were close to those of the principal PPO meridians (determined previously from near-apoapsis nightside magnetic data) for both systems, moving to somewhat earlier PPO phases by a few tens of degrees in the transport region. Comparison with magnetic oscillation phases determined directly from proximal pass data shows that electron density maxima occur ~30°–50° earlier than azimuthal field maxima for both systems, ~140°–160° earlier than colatitudinal field maxima for the northern system, nearer to antiphase than to leading quadrature, and ~50°–70° later than colatitudinal field maxima for the southern system, somewhat less than lagging quadrature.

1. Introduction

During the final phase of its Saturn orbital mission, between April and September 2017, the Cassini spacecraft made 22 proximal periapsis passes near noon approximately north-south through the equatorial gap between the inner edge of the innermost D ring of Saturn and the denser layers of the upper atmosphere, before being destroyed in the upper atmosphere pre-periapsis on the final orbit. These passes correspond to full spacecraft revolutions (Revs) 271–292, defined from apoapsis to apoapsis, and to final partial Rev 293. The data acquired on these passes have provided unique information on field and particle conditions on field lines passing through Saturn's equatorial ring system, building on the observations obtained on the single partial lower-latitude pass during Saturn orbit insertion (SOI) in 2004. In particular, the first in situ measurements of Saturn's near-equatorial planetary ionosphere were obtained, both directly from Langmuir probe data (Wahlund et al., 2018), as well as inferred from plasma wave emissions (Persoon et al., 2019). These data add significantly to previous remote sensing ionospheric observations derived from radio occultation measurements, lightning-induced radio emissions, and infrared emissions from ionospheric H_3^+ ions (e.g., Fischer et al., 2011; Kliore et al., 2014; O'Donoghue et al., 2013).

The proximal observations have revealed the presence of a layered ionospheric structure, with electron densities reaching peak values of $\sim 1.5 \times 10^4 \text{ cm}^{-3}$ at ~1,550 km altitude (above 1 bar), as observed on the final inbound pass in the northern hemisphere at the end of mission (Hadid et al., 2019). Above this, up to ~2,500 km, as observed on the final five full passes (Revs 288–292 with near-equatorial minimum altitudes between 1,632 and 1,712 km), the electron density was observed to fall relatively rapidly with altitude, with an e-folding scale height of ~250–500 km (Hadid et al., 2019; Morooka et al., 2019; Persoon et al., 2019).

© 2021. The Authors.

This is an open access article under the terms of the [Creative Commons Attribution License](https://creativecommons.org/licenses/by/4.0/), which permits use, distribution and reproduction in any medium, provided the original work is properly cited.

However, Langmuir probe data show that the electron density was significantly less than the positive ion density in this region, indicating the presence of a dusty photochemical equilibrium plasma dominated by heavy positive and negative ions (Morooka et al., 2019). The properties of this plasma are believed to be strongly affected by a substantial “ring rain” influx into Saturn’s primarily neutral hydrogen upper atmosphere of charged and neutral particles from Saturn’s rings (Connerney & Waite, 1984; Hamil et al., 2018; O’Donoghue et al., 2013, 2017). These particles consist of water, silicate, and organic (carbon-containing) grains, that were also directly detected on the proximal passes (Hsu et al., 2018; Moore et al., 2018; Mitchell et al., 2018; Perry et al., 2018; Waite et al., 2018). Investigation of the properties of this predominantly heavy ion layer by Shebanits et al. (2020) has shown that its electrical conductivity is increased by more than an order of magnitude compared with previous estimates, forming an extensive conducting layer ~300–800 km thick.

Above this region, between ~2,500 and ~4,000 km altitude, an inferred diffusive layer was then observed, in which the electron densities are equal to the positive ion densities within errors, falling somewhat more slowly in altitude with a scale height of ~500–800 km (Hadid et al., 2019; Morooka et al., 2019). Unlike the lower layer, the positive ions in this region are dominated by light species H^+ (protons) and H_3^+ . Above ~4,000 km the ionosphere then becomes a near-collisionless proton-electron plasma which varies slowly in altitude with a scale height (derived using northern hemisphere data) of ~4,500 km (Hadid et al., 2019; Persoon et al., 2019; Wahlund et al., 2018). Convective transport effects are likely to be prominent in this region, similar to the Earth’s plasmasphere. We note, however, that considerable pass-to-pass variability in electron density was found to occur within these upper regions, above ~3,000 km, by at least an order of magnitude.

At altitudes above ~12,500 km, magnetically mapping equatorially to Saturn’s outer dense B and A rings, evidence was also found from whistler wave data of a plasma cavity with electron densities as low as $\sim 0.1\text{--}1\text{ cm}^{-3}$ (Farrell et al., 2018), confirmatory of related observations during the SOI pass (Xin et al., 2006). Saturn’s B and A rings span radial distances between ~ 1.53 and $\sim 2.27 R_S$ in the equatorial plane, where R_S is Saturn’s 1 bar equatorial radius 60,268 km. It was inferred that the cavity is formed by equatorial absorption of ionospheric plasma by the dense ring environment, leading to continual outflow of ionospheric ions and electrons into the cavity regulated by an ambipolar potential of order ~ 1 V.

On the highest altitude proximal passes, those with periapsis altitudes above ~3,000 km (Revs 276–282 with minimum altitudes between 3,349 and 3,893 km), direct plasma effects associated with in-falling D ring dust grains were also observed in a restricted layer centered near the equator (Morooka et al., 2019; Wahlund et al., 2018). The tenuous innermost D ring spans equatorial radial distances $\sim 1.11\text{--}1.24 R_S$, corresponding to altitudes between ~6,600 and ~14,200 km (the tenuous C ring then lying between its outer edge and the inner edge of the dense B ring at $\sim 1.53 R_S$, corresponding to an altitude of ~32,000 km). Modest peaks in the ion density were found to occur in this equatorial layer, while electron densities were found to fall to values significantly less than the ion densities, again indicating the presence of a dusty plasma with significant negative charge on dust grains. Impacts of micron-sized dust grains on the Cassini electric field antennas were also found to occur in a narrow equatorial region on these orbits (Ye et al., 2018), though the plasma effects likely principally involve smaller more numerous grains, down to tens of nanometers in size.

These layered properties significantly condition the plasma-related observations on each of the proximal passes, though with considerable pass-to-pass variability in the diffusive layer and transport region as noted above. It should also be noted that altitude and latitude are generally strongly convolved on the proximal passes, as illustrated in the following section. Peak densities on each pass, however, usually lie close to periapsis, which occurred at latitudes between $\sim 5.3^\circ$ and $\sim 7.2^\circ$ in the southern hemisphere, at near-noon local times between 13.1 and 11.4 h (see, e.g., Table 1 of Cao et al., 2020). At post-periapsis southern latitudes larger than $\sim 15^\circ$ corresponding to altitudes above ~4,000 km, however, the electron densities were generally found to fall more rapidly with altitude than in the northern hemisphere, with an effective scale height along the spacecraft trajectory of ~2,500 km (Persoon et al., 2019). These plasma depletions have been shown to be associated with shadowing of the atmosphere/ionosphere by the dense A and B rings during the northern summer solstice conditions prevailing (Hadid et al., 2018; Wahlund et al., 2018). However, no significant depletions were observed at lower southern latitudes (and altitudes) associated with the shadows of the tenuous C and D rings, which thus appear to be effectively transparent to solar extreme ultraviolet (EUV) radiation.

Additional plasma phenomena observed on the proximal passes include the existence of a variable inter-hemispheric current system flowing in the region interior to the D ring field lines likely driven by shears in upper atmospheric flow (Dougherty et al., 2018; Khurana et al., 2018; Provan, Cowley, Bunce, et al., 2019; Agiwal et al., 2021), together with the presence of magnetic field modulations rotating near the planetary rotation period (~ 10.7 h) that are associated with the magnetosphere-wide planetary period oscillation (PPO) phenomenon (Provan, Cowley, Bradley, et al., 2019). As discussed further in Section 3, two such modulation systems with slightly different seasonally dependent periods are generally present, driven from the two polar ionospheric regions, which have been found to pervade the entire sub-auroral and ring-field regions down to lowest altitudes including the region interior to the D ring. In this study we examine whether the ionospheric electron density data observed in the ring field region and interior thereto also exhibit modulations at the PPO periods. We show that while there is no indication of such effects in the lower part of the photochemical equilibrium layer below $\sim 2,200$ km, modulations in the electron density are generally present in the diffusive layer and transport region above, contributing significantly to the pass-to-pass variations observed in these regions.

2. Trajectory and Related Physical Regimes

2.1. Cassini Proximal Trajectories

In this section we describe the spacecraft trajectory during the proximal passes, providing context for the physical regimes observed. Figure 1 shows two of the proximal passes projected into a meridian plane using cylindrical (ρ, z) coordinates, where ρ is the perpendicular distance from the planet's spin/magnetic axis, and z is distance along the axis positive northward. Specifically, we show the trajectories for Revs 276 (blue) and 290 (red), corresponding to the passes with the highest and lowest near-periapsis minimum altitudes, respectively, prior to the final partial orbit. The overall similarity of these passes is evident. The outer boundary of the planet (orange) depicted corresponds to the 1 bar spheroid with equatorial and polar radii of 60,268 and 54,364 km (1.0 and $\sim 0.902 R_S$), respectively. In each case the spacecraft passed from north to south (orbit inclination $\sim 62^\circ$ to the equator) across the entirety of the magnetic field region mapping to Saturn's rings (blue shaded region) crossing the equator (black dotted line) in the narrow gap between the inner edge of the D ring and the denser layers of the planet's atmosphere. The blue and red solid circles on the trajectories show the near-equatorial minimum altitude points on each Rev, 3,893 km at latitude -4.2° for Rev 276 and 1,632 km at latitude -4.9° for Rev 290, where the altitude values quoted are with respect to the normal to the 1 bar planetary surface (shown in the figure), that we employ to organize the electron density data throughout the paper. Due to the spheroidal geometry of the planet, the minimum altitude points are displaced marginally northward toward the equator from the near-noon southern hemisphere periapsis points, which for Rev 276 occurred at -5.7° latitude and 12.7 h local time (LT), and for Rev 290 at -7.0° latitude and 11.6 h LT.

The black arrowed lines in Figure 1 show planetary magnetic field lines derived from the dominant first three terms (dipole, quadrupole, and octupole) of the Cao et al. (2020) internal magnetic field model obtained from the proximal data, together with a ring current field determined from the Bunce et al. (2007) model for a typical subsolar magnetopause radius of $22 R_S$. The polar field lines have been drawn at 5° colatitude intervals from the northern pole between the planetary (z) axis and 30° , with their conjugate counterparts in the southern hemisphere, while being drawn to mark ring boundaries in the interior region where the field lines pass through Saturn's main ring system. Specifically, the outer regions shaded darker blue correspond to field lines passing through the denser A and B rings as marked in the figure, with the paler blue central gap between them corresponding to the Cassini Division. The inner ring region also shaded paler blue corresponds to the field lines passing through the more tenuous C and D rings, with the spacecraft trajectory crossing the equator just interior to the D ring inner boundary. The gray-shaded regions in the lower half of Figure 1 show the approximate region of solar EUV shadow formed in the noon meridian by the opaque A and B rings, under the northern near-solstice conditions prevailing. The region shaded in the figure corresponds specifically to the maximum solstice solar latitude of 26.73° (northern summer solstice occurred on May 24, 2017 during proximal Rev 275), but this value varied only marginally over the whole interval of proximal orbits. It can be seen that much of the post-periapsis outbound segment of the

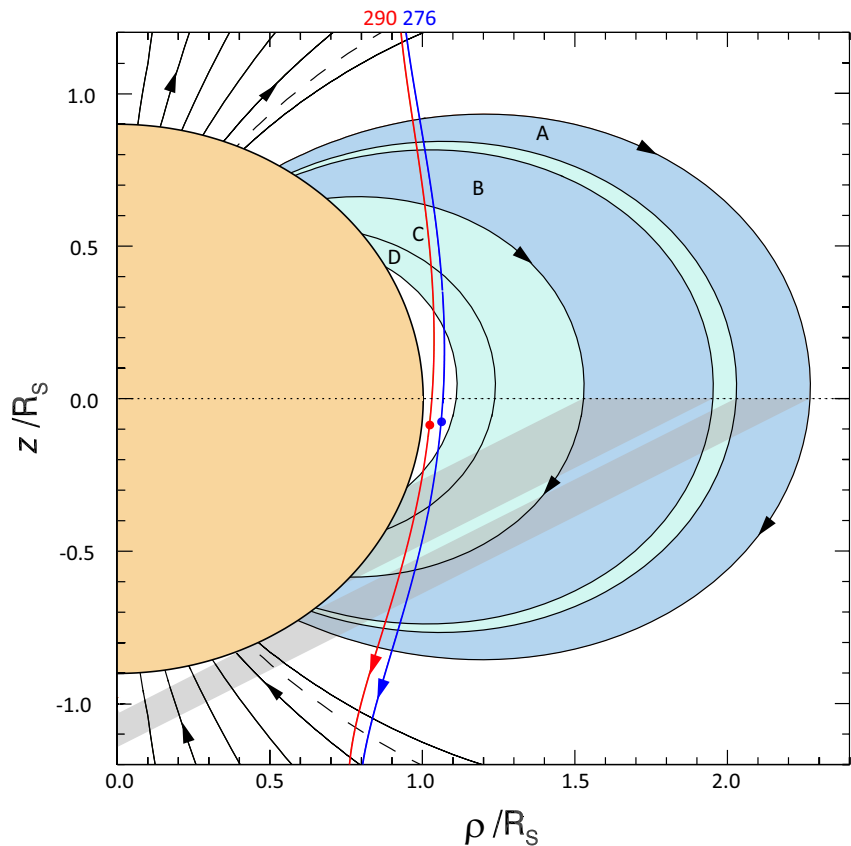


Figure 1. Proximal trajectories for Revs 276 (blue) and 290 (red), corresponding to the full passes with the highest and lowest near-periapsis minimum altitudes, respectively, projected into a magnetic meridian plane using cylindrical (ρ, z) coordinates, where ρ is the perpendicular distance from the planet's spin axis and z is distance along the axis positive northward (both in R_S). The near-periapsis points of minimum altitude are marked by the blue and red solid circles on the trajectories, with the spacecraft moving from north to south as indicated by the arrows. The orange spheroid depicts Saturn with an outer 1 bar surface with equatorial and polar radii of 60,268 (by definition 1 R_S) and 54,364 km, respectively. The black arrowed lines show planetary magnetic field lines (see text), where the polar field lines have been drawn at 5° colatitude intervals from the northern pole between the planetary (z) axis and 30° , with the black dashed line showing the field line passing through the orbit of Enceladus at $\sim 3.95 R_S$ in the equatorial plane. Conjugate field lines are shown in the southern hemisphere. In the interior region the field lines indicate ring field line boundaries. The outer regions shaded darker blue correspond to field lines passing through the denser A (equatorial radii 2.027–2.269 R_S) and B (1.527–1.951 R_S) rings, with the central paler blue gap showing the Cassini Division. The inner region shaded paler blue corresponds to field lines passing through the more tenuous C (1.239–1.527 R_S) and D (1.110–1.236 R_S) rings. The gray-shaded regions in the lower half of the figure show the approximate region of solar EUV shadow formed in the noon meridian by the A and B rings, specifically for a northern solstice solar latitude of 26.73° .

trajectory beyond southern latitudes of $\sim -15^\circ$ is in ring shadow, except for the gap corresponding to the Cassini Division.

2.2. Physical Regimes Traversed

Figure 2 provides an overview of the physical regimes observed on the proximal passes, where the trajectories are shown plotted versus latitude on the vertical axis and altitude (log scale) on the horizontal axis. The trajectories are color coded into overall Rev groups by the minimum altitude on each pass as shown at the top of the figure, as employed in data displays in subsequent figures. “Blue” Revs 276–282 have the highest minimum altitudes spanning between 3,349 and 3,893 km, followed by “green” Revs 271–274 and 288–292 spanning intermediate minimum altitudes between 2,651 and 2,942 km, while “red” Revs 288–292 reach lowest minimum altitudes near the end of mission spanning between 1,632 and 1,712 km. The brown

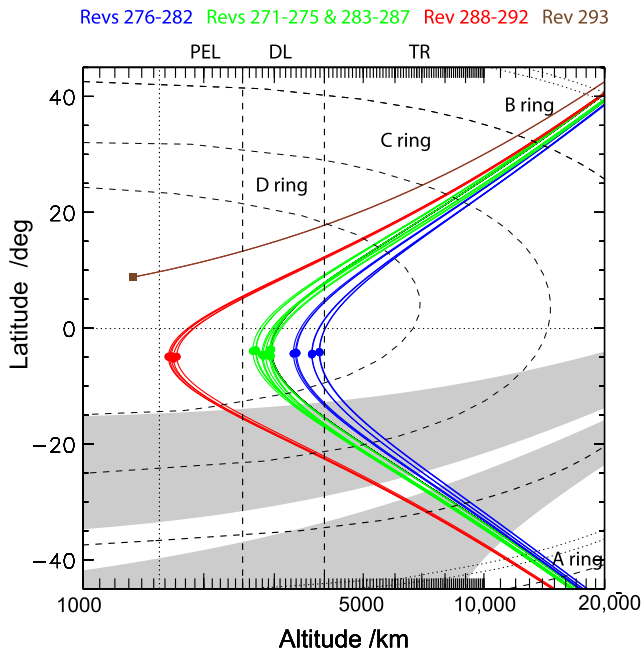


Figure 2. Plots of spacecraft latitude (degrees) versus altitude (km) on a log scale for all proximal passes, color-coded into three groups by minimum altitude on the pass as shown at the top of the plot. Highest altitude passes are shown blue (Revs 276–282), intermediate altitude passes are green (Revs 271–275 and 283–287), lowest altitude passes are red (Revs 288–292), and the final partial pass brown (Rev 293). Minimum altitude points on the passes are shown by similarly colored circles, while the lowest altitude from which data were acquired on the final pass is shown by the brown square. Spacecraft motion is from north to south. The vertical dotted line shows the altitude of maximum electron number density observed on the final pass (1,550 km), while the dashed lines mark the approximate upper boundaries of the dusty photochemical equilibrium layer (PEL) at 2,500 km and the light ion diffusive layer (DL) at 4,000 km, beyond which lies the near-collisionless hydrogen plasma transport region (TR). The black dashed curves show the boundaries of field lines mapping equatorially into Saturn’s main ring system as marked. The dotted lines map to the edges of the Cassini Division between the B and A rings. As in Figure 1, the gray-shaded regions in the lower half of the figure show the approximate region of solar extreme ultraviolet shadow formed in the noon meridian by the A and B rings at northern summer solstice. Overall, the figure encompasses essentially the whole region of spacecraft traversals of Saturn ring field line as shown in Figure 1.

trajectory shows the final partial Rev 293 ending at $\sim 9.6^\circ$ latitude in the northern hemisphere. The minimum altitude points on each trajectory are marked by the similarly colored circles, while the lowest altitude from which data were acquired on the final orbit is marked by the brown square. The vertical dotted line on the left of the figure indicates the altitude of maximum electron density observed on the final orbit (1,550 km), while the dashed lines indicate the approximate boundaries of the plasma physical regimes outlined in Section 1, specifically the dusty photochemical equilibrium layer below about 2,500 km (marked as PEL at the top of the figure), the diffusive layer (DL) dominated by light ions up to about 4,000 km, with the near-collisionless hydrogen plasma transport region (TR) beyond (Hadid et al., 2019; Morooka et al., 2019; Persoon et al., 2019; Wahlund et al., 2018). The black dashed curves show the boundaries of field lines mapping equatorially into the main ring system as marked, with the double dotted lines at upper and lower right showing the field lines mapping equatorially to the Cassini Division between the A and B rings. The gray-shaded region in the southern hemisphere shows the approximate region of solar EUV shadow as in Figure 1, formed in the noon meridian by the A and B rings at northern summer solstice. We note that the overall region shown, between $\pm 45^\circ$ latitude and to 20,000 km altitude encompasses essentially the whole of the proximal spacecraft traversals of the ring field region.

Figure 2 shows that only the last five full passes (red Revs 288–292), together with the final pass (brown Rev 293), traversed the dusty photochemical equilibrium layer, principally on field lines mapping equatorially inside the D ring. The earlier passes (blue and green Revs 271–287) spanned the width of the diffusive layer at minimum altitude, again observed mainly on field lines mapping inside the D ring, except for a segment lying on inner D ring field lines post-periapsis in the southern hemisphere. The transport region inbound spanned the whole of the ring field region to field lines mapping inside of the D ring, while outbound it generally only spanned the region beyond field lines mapping more centrally within the D ring. The strong correlation between latitude and altitude in the transport region shows that it is essentially impossible to separate latitude and altitude effects in this regime, as mentioned in Section 1. In the outer part of the ring field region, the A and B ring field lines (darker blue in Figure 1) are traversed within the transport region beyond $\sim 14,000$ km on the inbound passes and beyond $\sim 9,000$ km on the outbound passes. These field lines correspond to the region of very low plasma density reported by Farrell et al. (2018), likely due to ring absorption. Figure 2 also shows that the ring-shadowed region in the southern hemisphere corresponds principally to the transport region above $\sim 4,000$ km on the higher altitude (green and blue) outbound passes, while for the last five orbits (red) it includes all of the diffusive layer as well.

3. Electron Density Profiles and Their Dependence on PPO Phase

3.1. Overview of Electron Density Data

In Figure 3, we provide an overview of the electron density data employed, plotted versus altitude over the same range as Figure 2 in log-log format, where the vertical dashed lines again approximately delimit the various layers of the ionosphere as indicated at the top of the figure panels. The data are color coded by pass minimum altitude using the same scheme as in Figure 2, such that the blue-Rev data extend into the central diffusive region to $\sim 3,400$ km, the green-Rev data into the inner part of the diffusive layer to $\sim 2,700$ km,

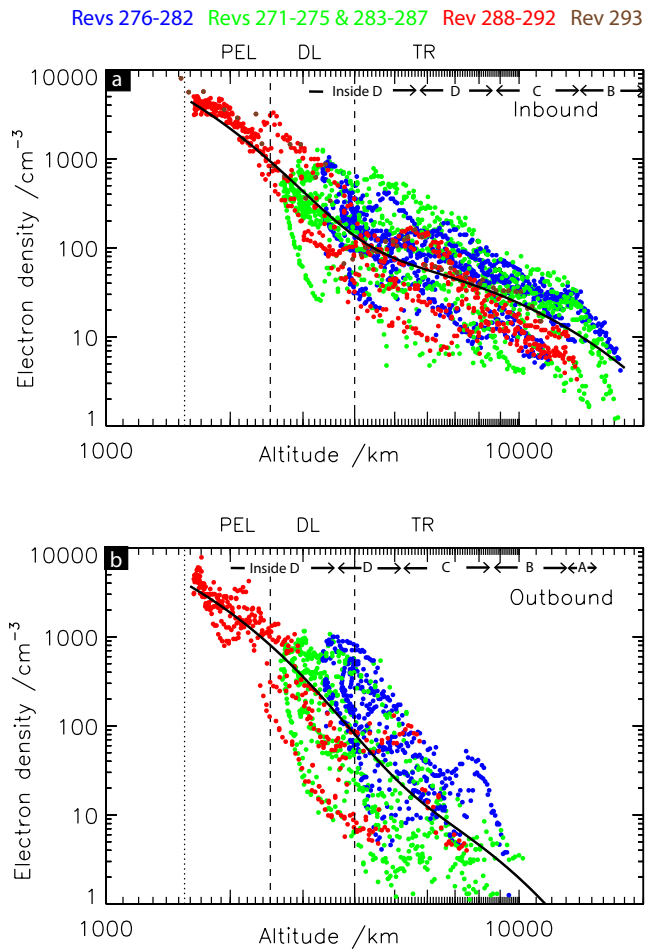


Figure 3. Plots of electron density (cm^{-3}) data determined from electric field plasma wave spectra by Persoon et al. (2019), plotted versus altitude above the 1 bar planetary spheroid (km) in log-log format, showing (a) data from the northern hemisphere and near-equatorial inbound passes to minimum altitude, and (b) data from the southern hemisphere outbound passes from minimum altitude (see Figure 2). As shown at the top of the figure the data are color-coded by Rev number as in Figure 2, such that blue data extends in to $\sim 3,350$ km, green to $\sim 2,650$ km, and red to $\sim 1,650$ km. The brown data shows values determined on the final pass to $\sim 1,500$ km. Also as in Figure 2, the vertical dotted and dashed lines indicate the approximate altitudes of the maximum electron number density and boundaries of ionospheric layers, respectively, as indicated above the figure panels. Based on Figure 2, we also indicate within each panel the approximate regime into which the field lines map in the equatorial plane. Specifically on the inbound passes the region inside the D ring is taken to extend out to 5,700 km, the D ring 5,700–8,700 km, the C ring 8,700–14,000 km, and the B ring 14,000–20,000 km. On the inbound passes the region inside the D ring is taken to extend out to 3,600 km, the D ring 3,600–5,200 km, the C ring 5,200–8,600 km, the B ring 8,600–13,000 km, and the A ring 13,000–15,500 km. The black curves show the scale height models given by Equation 1 fitted to the northern and southern hemisphere data by Persoon et al. (2019).

the red-Rev data to $\sim 1,600$ km just above the peak in the density profile, while only the brown final Rev data extend to just below the density peak to $\sim 1,500$ km.

The electron density data employed here are those derived by Persoon et al. (2019) from electric field wave spectra obtained by the Cassini Radio and Plasma Wave Science instrument (Gurnett et al., 2004). Specifically, the densities were derived from the electron plasma frequency upper cutoff in whistler mode emissions in low density regions either side of periapsis where the plasma frequency is smaller than the electron cyclotron frequency, and from upper hybrid emissions in higher density regions spanning periapsis. Although, as indicated in Section 1, essentially equivalent electron density values were also derived from Langmuir probe data, this set contains data gaps on six Revs when the probe lay in the spacecraft plasma wake. As will be clear from Section 3.2, the analysis undertaken here relies on combining together the data acquired on as many Revs as are available, hence the use here of the more continuous density data obtained from the wave observations.

In our analysis the data from each Rev are divided into the intervals before and after the near-periapsis minimum altitude points, termed the “inbound” and “outbound” data, respectively. Figure 3a shows the northern hemisphere and near-equatorial inbound data plotted in the format outlined above, while Figure 3b similarly shows the southern hemisphere outbound data. To provide physical context we also indicate in each figure panel the approximate regime into which the field lines map in the equatorial plane, from inside the D ring to the outer B and A rings (see figure caption for details). Although Figure 2 shows that these mappings vary a little from pass to pass, the regions shown nevertheless provide a useful indicator. The black lines superposed on the data show the scale height models fitted to the data by Persoon et al. (2019), given by

$$N_e = N_1 e^{-h/H_1} + N_2 e^{-h/H_2}, \quad (1)$$

where h is altitude, here plotted in log-log format. The values corresponding to the curve in Figure 3a are $N_1 = 80,915 \text{ cm}^{-3}$ with $H_1 = 545$ km, and $N_2 = 195 \text{ cm}^{-3}$ with $H_2 = 4,780$ km. Those corresponding to the curve in Figure 3b are $N_1 = 58,620 \text{ cm}^{-3}$ with $H_1 = 575$ km, and $N_2 = 135 \text{ cm}^{-3}$ with $H_2 = 2,360$ km. Although these values were derived specifically to fits of the data divided into northern and southern hemispheres, rather than inbound and outbound as employed here, the distinction is not significant in this context (see Figure 2). We note that at the lower altitudes in the photochemical equilibrium and lower diffusive layers the density values are similar in the two regimes, falling relatively rapidly with altitude with an overall scale height of ~ 500 km. Above this in the upper diffusive layer and transport region, the values fall less rapidly with altitude. The effective scale height is $\sim 5,000$ km for the inbound data, but smaller at $\sim 2,500$ km for the outbound data, associated with a more rapid decrease with altitude (and latitude) in the southern hemisphere compared with the northern hemisphere. This asymmetry is connected with the effect of ring shadow in the southern hemisphere, as discussed in Sections 1 and 2 (Figures 1 and 2). The density values then fall to very low values, $\sim 10 \text{ cm}^{-3}$ and below, at altitudes inbound and outbound corresponding to field lines mapping equatorially to the B ring as discussed in Section 1.

A key point arising from Figure 3, however, is the degree of scatter in the density values at a given altitude. While there is relatively little pass-to-pass variability in the density in the photochemical equilibrium layer,

particularly in the inbound data, the scatter increases rapidly to at least a factor five in the lower diffusive layer, and further to an order of magnitude or more in the transport region. That these variations are not principally due to pass geometry is seen in the fact that the data of all colors tend to be spread approximately equally across the band of scattered values at a given altitude, particularly in the inbound data, though there appears to be some red to green to blue layering associated with increasing density in the outbound data that is, likely due to ring shadow effects (Figure 2). Here we investigate to what extent the more general scatter present may be related to density modulations associated the PPO systems.

3.2. Proximal Pass Magnetic Field PPOs on Ring Region Field Lines

In a recent study Provan, Cowley, Bradley, et al. (2019) examined the magnetic field data obtained during the Cassini proximal passes, and showed that the quasi-sinusoidal field oscillations near the planetary rotation period that pervade Saturn's magnetosphere extend throughout the region of ring field lines essentially to periapsis. In fact the usual two systems of perturbations were found to be present, rotating with slightly differing seasonally dependent periods, one associated with the northern hemisphere but extending into the southern, the other associated with the southern hemisphere but extending into the northern.

During the proximal orbit interval, the periods, determined from the oscillations observed on these orbits in intervals adjacent to apoapsis on the nightside, were found to be near-constant and equal to 10.792 h for the northern system and 10.679 h for the southern system (Provan et al., 2018), with overall uncertainties of order ± 0.0005 h ($\sim \pm 2$ s). The global phases of the northern (N) and southern (S) systems employed here, $\Phi_{N,S}(t)$, define the azimuthal angles of the prime meridians of the two PPO systems with respect to the Sun, measured around the planetary rotation axis from noon positive in the sense of planetary rotation, as the systems rotate with time t at the above periods (Equations 29a and 29b of Provan et al., 2018). The azimuth of an observer relative to each system is then defined by the local phases, $\Psi_{N,S}$, given by

$$\Psi_{N,S}(\varphi, t) = \Phi_{N,S}(t) - \varphi, \quad (2)$$

where φ is the azimuth of the observation point (spacecraft) measured similarly from noon. The prime meridians of each system (where $\Psi_{N,S} = 0^\circ$ modulo 360°) are those in which the perturbation fields in the near-equatorial quasi-dipolar magnetosphere (outside the ring region to $\sim 12 R_S$) point radially outward from the planet. The radial perturbation fields in this regime thus oscillate as $\sim \cos \Psi_{N,S}$, while the azimuthal fields oscillate as $\sim \sin \Psi_{N,S}$, associated with an overall rotating quasi-uniform perturbation field in this outer equatorial region. The colatitudinal perturbation fields oscillate as $\sim -\cos \Psi_N$ for the northern system (the perturbation field lines closing over the northern polar region), and as $\sim \cos \Psi_S$ for the southern system (the perturbation field lines closing over the southern polar region). Typical amplitudes are ~ 1 – 2 nT. With regard to the relative strengths of the two systems, analysis of both near-apoapsis and near-periapsis data suggest north/south system amplitude ratios of ~ 1.3 – 1.4 during the proximal orbit interval (Provan, Cowley, Bradley, et al., 2019; Provan et al., 2018), so that the northern system was the stronger of the two, but not by a large factor.

The magnetic oscillations observed in the ring field region on the periapsis passes will be discussed in detail in Section 4.4, but briefly Provan, Cowley, Bradley, et al. (2019) found that these were stronger in the pre-noon northern hemisphere inbound data than in the post-noon southern hemisphere outbound data for both systems, though with the northern system being moderately stronger than the southern system in both regimes in conformity with the above discussion. They also found that the oscillations moved to somewhat "earlier" phases compared with the outer magnetosphere and auroral regions, generally reaching near-quadrature within the ring region. Typical amplitudes were ~ 2 – 6 nT for the azimuthal and co-latitudinal field components (tangent to Saturn's surface), though smaller and generally indeterminate for the radial component (normal to Saturn's surface).

In order to search for PPO effects in the electron density data we note that the time scale for each proximal periapsis pass across the entire ring field region (Figure 1) was ~ 1 h, much shorter than the PPO rotation periods. To discern such effects we must therefore compare density values determined from pass to pass under conditions of differing PPO phases Ψ_N and Ψ_S . With the northern and southern periods given above (10.792 and 10.679 h, respectively), the beat period of the two systems was 42.5 ± 0.3 days, such that the ~ 140 days interval of proximal orbits comprised ~ 3.5 beat cycles of the two oscillations. Consequently, the

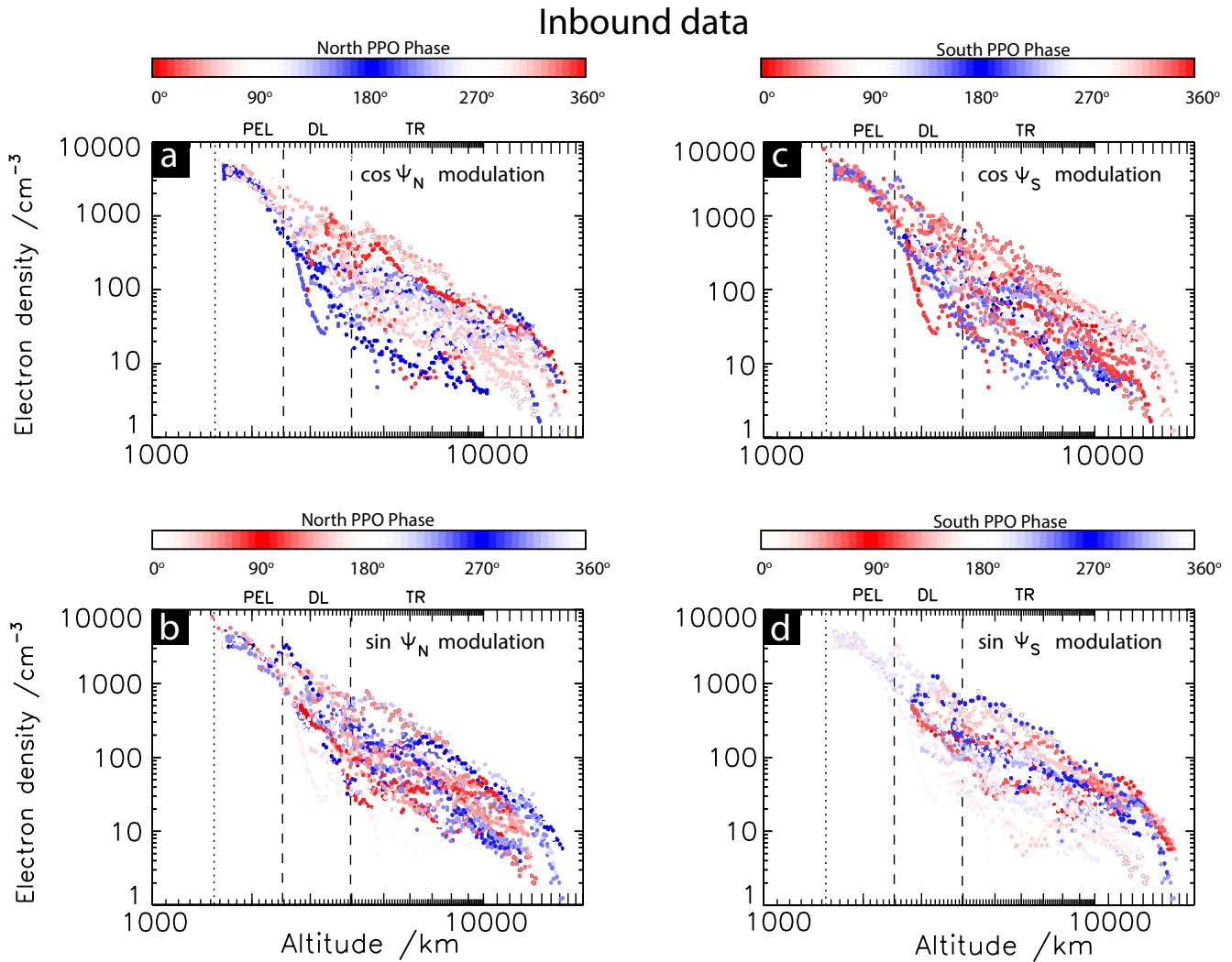


Figure 4. Plots of the electron density (cm^{-3}) on the inbound proximal passes in a similar log-log format to Figure 3a, but now color-coded by the phases of the northern and southern planetary period oscillation (PPO) systems, Ψ_N and Ψ_S , derived by Provan et al. (2018) from nightside near-apoapsis data. Specifically, panels (a and b) show the data color-coded in red and blue according to $\cos \Psi_N$ and $\sin \Psi_N$, respectively, as indicated at the tops of these panels. Panels (c and d) similarly show the same data color-coded in red and blue according to $\cos \Psi_S$ and $\sin \Psi_S$, respectively.

phases of the two systems were not correlated with each other over the proximal interval as a whole, such that the two oscillations can be analyzed separately (see discussion in Provan, Cowley, Bradley, et al., 2019). We also note that in view of the differences in the electron density values seen in Figures 3a and 3b, separate analyses of the inbound (northern and equatorial) and outbound (southern) data are required, beginning in the next section with an initial survey of the inbound data.

3.3. PPO Modulations in Inbound Electron Density Data

To provide an initial view as to whether PPO-related effects are present in the inbound density data, in Figures 4a and 4b we have color coded the data in Figure 3a by the values of the cosine and sine of the northern phase, Ψ_N , respectively, as shown by the color bars at the top of each panel. Thus in Figure 4a data obtained under conditions where $\cos \Psi_N$ is positive or negative are colored in shades of red or blue, respectively, while in Figure 4b data obtained under conditions where $\sin \Psi_N$ is positive or negative are similarly colored in shades of red or blue, respectively. Density values varying as $\sim \cos \Psi_N$ would then show red values larger than blue in Figure 4a, while values varying as $\sim \sin \Psi_N$ would similarly show red values larger than blue in

Figure 4b. Examining Figure 4a, there is clear color separation with red greater than blue in the diffusive layer above $\sim 2,500$ km and in the lower transport region to at least $\sim 5,000$ km, indicating a variation as $\sim \cos \Psi_N$ in these regions. We note that while the altitude values quoted in this section may be considered as somewhat subjective rough values determined by visual inspection of these figures, in Section 4.3 they will be validated by the results of quantitative analysis. In Figure 4b there is little indication of an effect within the diffusive layer, while a weaker color separation appears in the transport region to $\sim 6,000$ km, but now with blue data greater than red, indicating a variation as $\sim -\sin \Psi_N$. Expressing the latter result in terms of a phase lag Δ_N relative to Ψ_N , that is,

$$n_e \sim \cos(\Psi_N - \Delta_N) = \cos \Delta_N \cos \Psi_N + \sin \Delta_N \sin \Psi_N, \quad (3)$$

it can be seen that when $\cos \Delta_N$ is positive and $\sin \Delta_N$ negative, this implies that Δ_N lies in the phase quadrant between 270° and 360° (equivalent to -90° – 0°). These results thus indicate that in the inbound diffusive layer and in the transport region to $\sim 7,000$ km, modulation of the electron density at the northern PPO period is present, with peak densities occurring near the principal meridian of the northern system in the diffusive layer, but moving to somewhat earlier phases in the transport region. Significant modulation is not evident in the dusty photochemical equilibrium layer, but because only six passes contribute to the data in this region (Revs 288–293, see Figure 2), the phase coverage of these data needs detailed examination, as will be discussed in Section 4.2.

These same inbound density data can equivalently be examined for modulations at the southern PPO period, it being noted from Section 3.2 that because the overall proximal pass interval corresponds to more than ~ 3 beat cycles of the two oscillations, their relative phases are essentially uncorrelated over the data set as a whole. Modulation due to one system then simply introduces “noise” when analyzed for periodicities at the period of the other system. Results for modulations as $\sim \cos \Psi_S$ and $\sim \sin \Psi_S$ are shown in Figures 4c and 4d, respectively, in the same format as Figures 4a and 4b. Although the coverage with respect to the southern phase is very uneven as a consequence of an accidental relation between the southern PPO period and the orbital period such that the southern phase changed by approximately 180° from one pass to the next, Figure 4c again provides evidence of modulation as $\sim \cos \Psi_S$ in the upper part of the diffusive layer above $\sim 3,250$ km and in the transport region up to $\sim 10,000$ km, while the coverage in Figure 4d appears insufficient to provide a clear indication of a $\sin \Psi_S$ dependency. The results in Figure 4c nevertheless indicate the presence of modulation of the northern inbound electron density at the southern PPO period, with a phase such that maxima occur near the prime meridian of the southern system. There is again no indication of modulation in the photochemical equilibrium layer below $\sim 2,500$ km. In the diffusive layer and transport regions, however, these results suggest similar modulation responses of the northern inbound electron densities to both the northern and southern PPO systems, with maxima occurring near the principal meridians of both systems as determined from nighttime near-apoapsis data by Provan et al. (2018).

3.4. PPO Modulations in Outbound Electron Density Data

Figure 5 shows the outbound electron density data color coded by the cosine and sine of Ψ_N and Ψ_S in the same format as Figure 4. It can be seen in Figures 5a and 5b that density modulations with respect to Ψ_N appear to be present above $\sim 3,500$ km in the upper diffusive layer to $\sim 6,000$ km in the transport region, with a $\sim \cos \Psi_N$ dependency throughout, and with a $\sim -\sin \Psi_N$ dependency appearing above $\sim 4,000$ km in the transport region. As for the inbound data in Figures 4a and 4b, these indicate a modulation phasing such that density maxima occur near the prime meridian of the northern system in the diffusive layer, moving to somewhat earlier phases in the transport region. There is again no evidence of PPO-related modulations at lower altitudes in the photochemical equilibrium layer. Unlike Figures 4c and 4d, however, Figures 5c and 5d do not provide clear indication of density modulations in the outbound data with respect to Ψ_S . A more quantitative analysis is required to take the discussion further, presented in the next section.

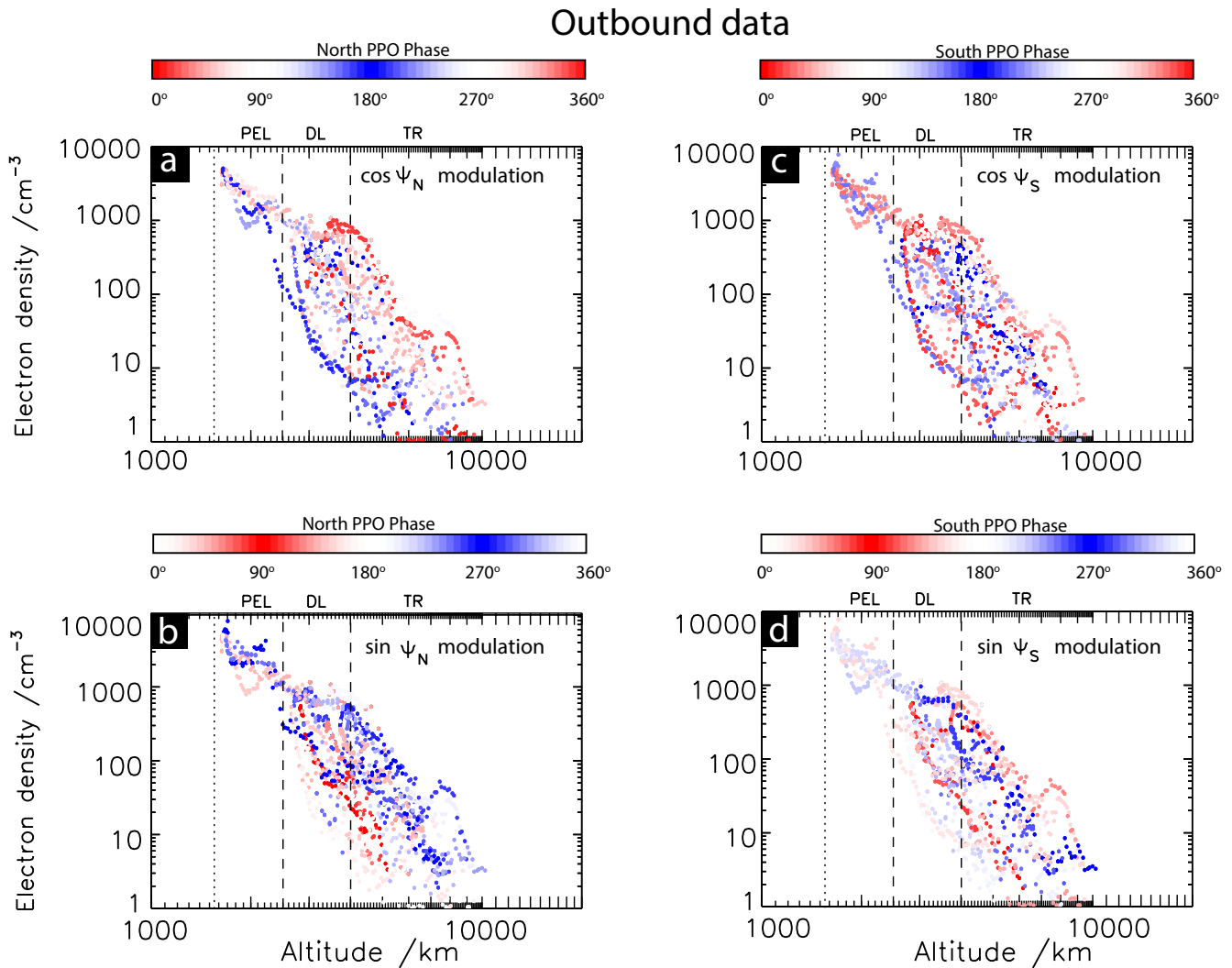


Figure 5. As for Figure 4, but for the electron density on the outbound proximal passes.

4. Sinusoidal Fits to the Density Data as Functions of PPO Phase

4.1. Sinusoid Fitting to the Electron Density Data

We now quantify the electron density modulations by fitting a sinusoidal function of PPO phase to data divided into given altitude ranges, separately for the inbound and outbound data. Specifically, we fit the following sinusoid to the logarithm (base 10) of the density

$$\log n_e(\Psi_{N,S}, h) = M_{N,S}(h) + A_{N,S}(h) \cos(\Psi_{N,S} - \Delta_{N,S}(h)), \quad (4)$$

where h is altitude above 1 bar as employed in Figures 2–5, and the fit parameters are the mean value $M_{N,S}(h)$ of the logged density (equal to the mean of the logged data if uniformly sampled in phase), the oscillation amplitude $A_{N,S}(h)$, and the phase lag $\Delta_{N,S}(h)$. We also calculate the root mean square (RMS) deviation $d_{N,S}$ of the logged density values from the fitted line. The electron density data are divided into suitably chosen non-overlapping ranges of altitude, with the logged data values from each contributing Rev first being averaged in value and phase (the phase being almost constant for a given Rev), with the fit being applied to these averaged values. The fit employs least squares minimization, with uncertainties determined using the “jackknife” statistical resampling method (see Provan, Cowley, Bradley, et al., 2019, section 4.1.1 and references therein). Results are presented in terms of the mean value of the density $\langle n_{e,N,S} \rangle$ in a given height range

$$\langle n_{eN,S} \rangle(h) = 10^{M_{N,S}(h)}, \quad (5a)$$

expected to be near-equal for the separate analyses with respect to the northern and southern phases, the factor $f_{AN,S}$ by which the density is modulated at that altitude with respect to the corresponding PPO phase

$$f_{AN,S}(h) = \frac{n_{e \max}(h)}{n_{e \min}(h)} = 10^{2A_{N,S}(h)}, \quad (5b)$$

and the phase lag $\Delta_{N,S}$. We also calculate the factor related to the RMS deviation of the logged data about the fitted curve

$$f_{dN,S}(h) = 10^{d_{N,S}(h)}. \quad (5c)$$

Comparison of this value with the PPO modulation factor $f_{AN,S}$ given by Equation 5b indicates the extent to which the electron density variations in a given height range are governed by PPO modulations as opposed to other sources. PPO modulation of the density contributes significantly to the overall variability if $f_{AN,S} \gtrsim f_{dN,S}$, that is, if the peak-to-peak PPO modulation is comparable with or greater than the RMS deviation of the data from the fitted line.

4.2. Illustrative Fits to the Density Data

Figures 6–8 show some illustrative individual fits to the data in the three ionospheric regimes identified in Figures 2–5. In each panel the electron density data from a specified altitude range are color-coded by Rev number as in Figures 2 and 3, and plotted on a log scale versus PPO phase. The altitude ranges are chosen to be representative of those employed in the overall analysis as discussed in Section 4.3 below. Two cycles of phase are shown in each plot in order to better visualize the continuity of the data. The means of the logged density values and PPO phases from each contributing Rev are shown by black crosses overplotted on the data in the first phase cycle of each panel, while the best-fit line fitted to these mean values is shown by the black dashed curve, with the mean value shown by the horizontal black dotted line. Fit parameters with uncertainty ranges are given in each panel, specifically the mean value $\langle n_e \rangle$ (Equation 5a), the PPO modulation factor f_A (Equation 5b), the phase lag Δ , and the RMS deviation factor f_d (Equation 5c).

We begin in Figure 6 by showing fits to the data in the 200 km range centered on 3,400 km lying in the upper half of the diffusive layer, where the results of the red/blue display in Figures 4 and 5 suggest that PPO modulations may be reasonably clear, certainly for northern system modulations of the inbound data. Figure 6a shows data from the inbound passes plotted versus northern PPO phase Ψ_N . A clear modulation by a factor $f_{AN} \approx 4.96^{+2.48}_{-1.65}$ is evident, compared with a significantly smaller RMS deviation factor $f_{dN} \approx 1.75$. The peak density occurs at northern phase $\Psi_N = \Delta_N \approx 8.5^\circ \pm 15.6^\circ$, well localized to within a $\sim 30^\circ$ phase sector containing the prime meridian, consistent with the strong red greater than blue data separation at the corresponding altitude in the “cos plot” in Figure 4a, together with the lack of clear separation in the “sin plot” in Figure 4b. It is thus clear that modulation by the northern PPO system makes a significant contribution to the overall variability of the density data in this regime. Figure 6b shows the same data plotted versus southern PPO phase Ψ_S . While a larger scatter is present, due in part to the northern system modulation, evidence for a weaker modulation with respect to the southern PPO phase is nevertheless indicated by the PPO factor $f_{AS} \approx 2.06^{+1.3}_{-0.8}$, compared with a marginally larger RMS deviation factor $f_{dS} \approx 2.14$. Similar to the northern system modulation, peak density occurs at phase $\Psi_S = \Delta_S \approx 9.2^\circ \pm 44.6^\circ$, now localized by this analysis only within a quadrant of phase centered near the prime meridian, consistent with the results of the red-blue display in Figures 4c and 4d.

Figures 6c and 6d show data from the same altitude range on the outbound passes in the same format. These data show a greater overall scatter compared with those on the inbound passes, together with a displacement of the data on the final set of Revs (red) to lower values (Figure 3). The latter separation is likely due to ring shadow effects, since Figure 2 indicates that in this altitude range on the outbound passes the red data will correspond to shadow, the green data close to the edge of shadow, and the blue data to sunlight. To maintain maximum phase coverage all these data are analyzed together, though recognizing that variable shadow-related effects such as those seen here will somewhat increase the RMS deviation of the best-fit sinusoids. Despite these effects, northern PPO phase modulation can indeed be discerned in Figure 6c,

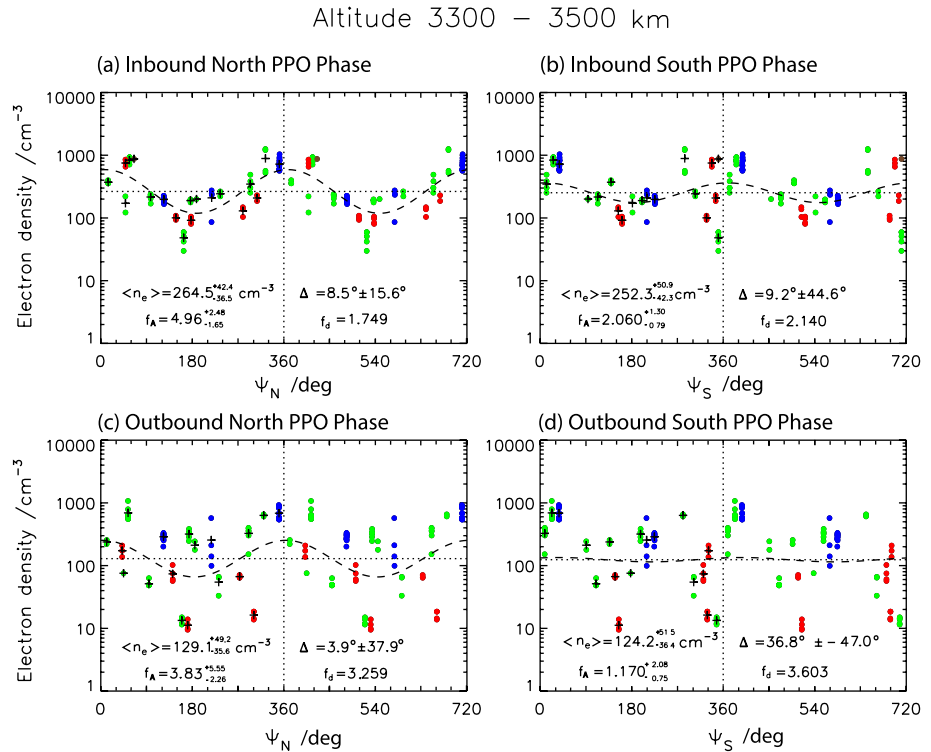


Figure 6. Illustrative individual fits to electron density data in the diffusive layer of Saturn’s ionosphere, specifically the 200 km altitude range centered on 3,400 km. In each panel the density data are color-coded by Rev number as in Figures 2 and 3, and plotted on a log scale versus planetary period oscillation (PPO) phase. Panels (a and b) show data from the inbound passes plotted versus the northern Ψ_N and southern Ψ_S PPO phases, respectively. Panels (c and d) similarly show data from the outbound passes plotted versus the northern and southern PPO phases, respectively. Two cycles of phase are shown in each figure to aid visualization of data continuity. Overplotted black crosses in the first phase cycle in each panel show the means of the logged density values and phases for each contributing Rev, which are the values employed in the sinusoid fit. The best fit sinusoid is shown by the black dashed curve, with the mean value shown by the horizontal black dotted line. Fit parameters with uncertainty ranges are given in each panel (see Section 4.1 Equations 5a–5c).

yielding a northern system modulation factor $f_{A_N} \approx 3.83^{+5.55}_{-2.26}$ now only modestly larger than the RMS deviation factor $f_{d_N} \approx 3.26$, which is significantly larger than the RMS deviation factor for the equivalent inbound data in Figure 6a. Peak density occurs at phase $\Psi_N = \Delta_N \approx 3.9^\circ \pm 37.9^\circ$ still near the prime meridian of the northern system, in accord with Figures 5a and 5b. However, these same data plotted versus the southern PPO phase in Figure 6d provide no evidence of such modulation at this altitude, as in Figures 5c and 5d. The uncertainty range of f_{A_S} as determined by the jackknife procedure encompasses unity, consistent with no modulation effect, while the RMS deviation factor $f_{d_S} \approx 3.60$ is large.

Figure 7 provides a similar illustration of PPO dependency at higher altitudes in the transport region, specifically in the 200 km altitude range centered on 4,600 km. Figure 2 indicates that all of the outbound data in this case will lie in the shadow region, such that there are no obvious “displacement” effects in these data as there were in Figure 6. The northern hemisphere inbound data shown in Figures 7a and 7b provide results that are similar to those in the inbound diffusive layer in Figures 6a and 6b, with clear evidence for northern PPO modulations together with more marginal evidence for southern PPO modulations, respectively. The northern and southern modulation factors $f_{A_N} = 4.67^{+3.89}_{-2.12}$ and $f_{A_S} = 1.92^{+1.47}_{-0.83}$ are both a little smaller than those in the diffusive layer, while the RMS deviation factors $f_{d_N} \approx 2.35$ and $f_{d_S} \approx 2.65$ are both a little larger. In conformity with the red/blue displays in Figures 4a–4d, showing red data greater than blue in the “cos” plots and blue greater than red in the “sin” plots, the density maxima now occur at the somewhat “earlier” phases $\Delta_N \approx -35.1^\circ \pm 21.8^\circ$ and $\Delta_S \approx -11.8^\circ \pm 66.3^\circ$. The southern hemisphere outbound data in Figures 7c and 7d again have similarities with their diffusive layer counterparts in Figures 6c and 6d, but now the

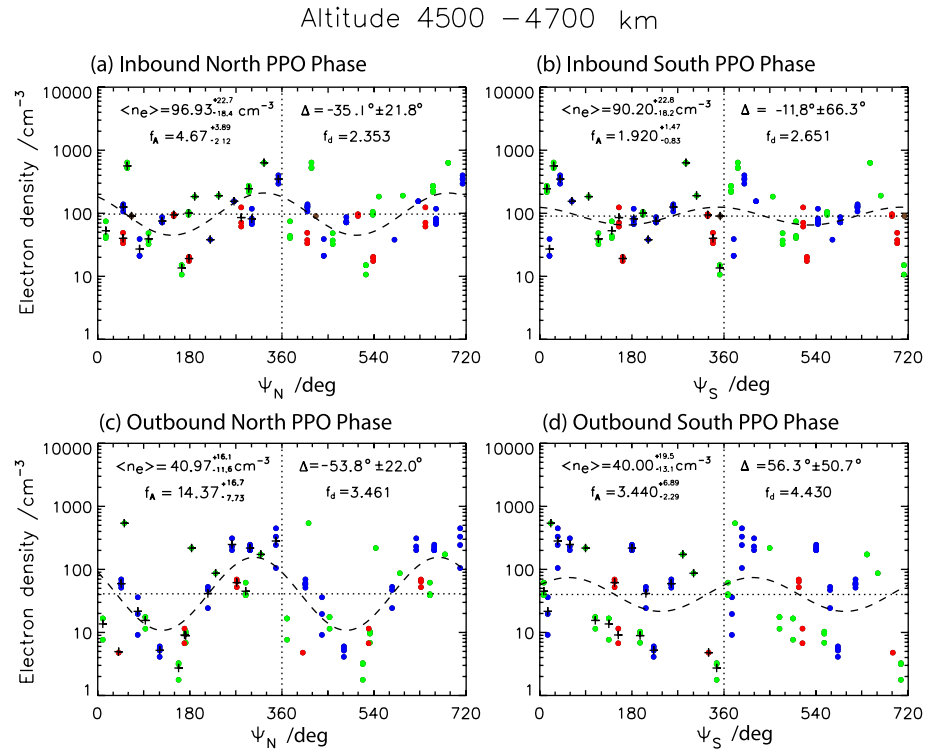


Figure 7. As for Figure 6 but for electron density data from the transport region of Saturn’s ionosphere, specifically the 200 km altitude range centered on 4,600 km.

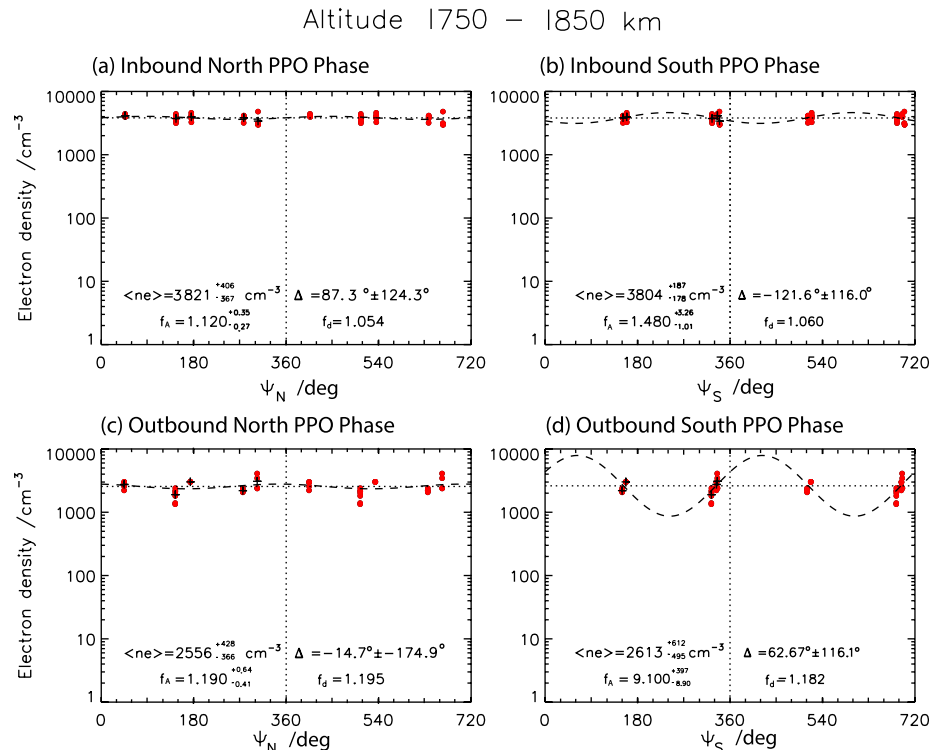


Figure 8. As for Figure 6 but for electron density data from the photochemical equilibrium layer of Saturn’s ionosphere, specifically the 100 km altitude range centered on 1,800 km.

northern system modulations are rather stronger with $f_{AN} \approx 14.37^{+16.7}_{-7.73}$ compared with a RMS deviation factor $f_{dN} \approx 3.46$, with only marginal evidence of a southern system modulation with $f_{AS} \approx 3.44^{+6.89}_{-2.29}$ relative to a RMS deviation factor $f_{dS} \approx 4.43$.

Figure 8 provides an overview of fit data in the photochemical equilibrium layer, specifically for the 100 km range centered on 1,800 km. In this range only the data from the final five full Revs 288–292 (red) contribute, all of which will be in sunlight on the outbound passes (Figure 2). However, five values are in general too few to yield well-determined sinusoid fits. This issue is compounded for the case of the southern phase data in Figures 8b and 8d by the repetitive nature of the pass-by-pass phase values, $\sim 180^\circ$ apart, resulting from the accidental relationship between the southern PPO period and the orbit period during the proximal orbit interval mentioned in Section 3.3. However, it can be seen from these plots that there is essentially no significant PPO modulation in the density values on the inbound passes, consistent with the much tighter grouping of the data in this region in Figure 3a, varying typically by less than a factor of ~ 2 at a given altitude, compared with the order of magnitude variations at a given altitude in the inbound diffusive layer and transport region. While this conclusion requires a caveat with regard to southern PPO system modulations due to the limited southern phase coverage, we note that the observed phases are near to those at which maxima and minima occur in the density modulations in the diffusive layer and transport region in Figures 6 and 7b, respectively, yet no such differences are observed in Figure 8b. The density values are slightly more variable on the outbound passes, as seen in Figure 3b, but again no clear PPO modulations are evident. Rather, all the PPO modulation factors $f_{AN,S}$ are consistent with unity (i.e., no effect), including the spuriously large value determined from the ill-conditioned “best fit” in Figure 8d, while the uncertainties in the $\Delta_{N,S}$ phase values all exceed $\pm 115^\circ$, that is, essentially indeterminate. These results thus demonstrate an overall lack of significant PPO-related modulations in this lower altitude ionospheric layer.

4.3. Overview of Results

We now discuss overall results from the sinusoidal fits, beginning in Figure 9 with results for the northern and equatorial inbound data. Figures 9a–9c show fit results for the analysis with respect to the northern PPO phase Ψ_N , plotted versus altitude on a log scale as in Figures 2–5, where the vertical dotted and dashed lines delimit the various layers of the ionosphere as in the latter figures. As in Figure 3, we also indicate near the top of these figures the ring regime into which the field lines at a given altitude map in the equatorial plane. Figure 9a shows the mean value of the electron density $\langle n_{eN} \rangle$ (Equation 5a), overplotted on the corresponding profile determined by Persoon et al. (2019) shown previously in Figure 3a (solid line). Figure 9b shows both the PPO modulation factor f_{AN} (solid circles with uncertainty estimates [Equation 5b]) and the RMS deviation factor f_{dN} (open triangles [Equation 5c]) for comparison, while Figure 9c shows the phase angle Δ_N . The solid circles showing the PPO modulation factor f_{AN} in Figure 9b are plotted red if f_{AN} is larger than the RMS deviation factor f_{dN} , indicating a PPO modulation comparable with or larger than the scatter of the data about the fitted line, and are shown black otherwise. Figures 9d–9f show corresponding results for the same inbound data but now similarly analyzed with respect to the southern PPO phase Ψ_S . In both panels the data have been divided into equally spaced non-overlapping ranges of logged (base 10) altitude, with 40 ranges per decade, providing an approximately constant ~ 4 electron density data values per contributing Rev. We note that the width of the altitude range at altitude h , given by $\Delta h = (10^{1/N} - 1)h$ where $N = 40$ is the number of ranges per decade, is consistent with the ranges employed in the example fits shown in Figures 6–8. Specifically, range width Δh increases from ~ 100 km at $\sim 1,800$ km altitude, as employed in Figure 8, to ~ 200 km at $\sim 3,400$ km altitude, as employed in Figure 6. We also note that at the highest altitudes in the transport region above $\sim 13,000$ km where the electron densities drop to low values (Figure 3), we do not show results for ranges where there are data from 12 or fewer contributing Revs (i.e., approximately half or less). The lack of phase coverage under these circumstances renders the results unreliable with very large uncertainties. The coverage thus extends essentially to the inner edge of the B ring field lines. The same issue also afflicts the results in the photochemical equilibrium layer at lowest altitudes, of course, where data from only 5 or 6 Revs are available (Figure 2). However, these fit results have been included for completeness given the discussion of these data in Section 4.2 in respect of Figure 8.

Examining the results for the inbound data in Figure 9, it is first noted that the density profiles in Figures 9a and 9d derived from the two analyses are essentially equal within uncertainties as expected, and also very

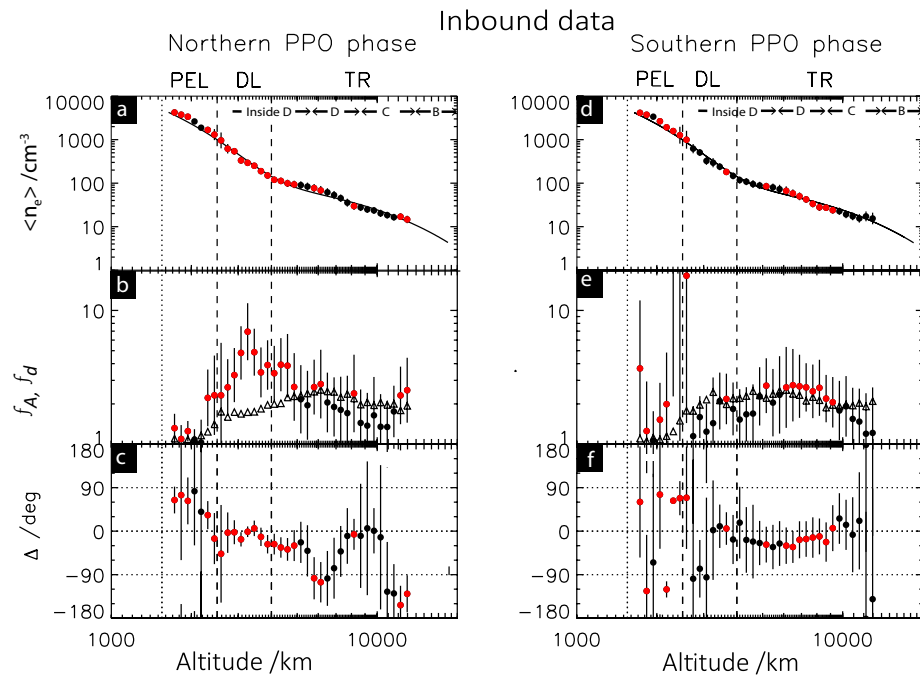


Figure 9. Overview of sinusoidal fit results for the northern hemisphere and equatorial region inbound electron density data with respect to the northern planetary period oscillation (PPO) phase Ψ_N in panels (a–c), and with respect to the southern PPO phase Ψ_S in panels (d–f), plotted versus altitude on a log scale. The vertical dotted and dashed lines indicate ionospheric altitude regimes as in Figures 2–5, while as in Figure 3 the horizontal arrows in panels (a and d) give an approximate indication of the ring regime into which the field lines at a given altitude map in the equatorial plane. The fit parameters are derived using density data in non-overlapping altitude ranges equally spaced in logged altitude, with 40 ranges per decade, such that each range contains a near constant number of 4 density values per contributing Rev. Panels (a and d) show the mean value of the electron density $\langle n_{e,N,S} \rangle$ (cm⁻³) from the two analyses, near equal as expected, overplotted on the corresponding northern model profile (Equation 1) determined by Persoon et al. (2019) (solid line). Panels (b and e) show both the PPO modulation factors (solid circles with uncertainty estimates) and the RMS deviation factors $f_{d,N,S}$ (open triangles), while panels (c and f) show the phase lags $\Delta_{N,S}$. In panels (b and e) the PPO modulation factors are plotted as red solid circles if $f_{A,N,S} \geq f_{d,N,S}$, and are plotted as black solid circles otherwise. In the higher altitude regime (above ~5,000 km) results are shown only if the number of contributing Revs exceeds 12 (i.e., more than approximately half the total), due to insufficient phase coverage leading to highly uncertain results for smaller numbers.

similar to the corresponding model profile determined previously by Persoon et al. (2019) (Equation 1). More significantly here, in line with the discussion in Section 4.2, the results for the northern PPO modulation factor f_{A_N} in Figure 9b show that the northern modulation is consistent with unity (i.e., no effect) in the photochemical equilibrium layer below ~2,200 km (Figure 8a), peaks at a factor of ~7 at ~3,200 km near the center of the diffusive layer (Figure 6a), and then falls in the transport region (Figure 7a) back to values consistent with unity by ~7,000 km. Comparison with the RMS deviation factor f_{d_N} indicated by open triangles in Figure 9b shows that the northern PPO modulation is the dominant effect in the density variability in the diffusive layer, but drops to become comparable with and less the RMS modulation factor ~2–3 in the transport layer at altitudes above ~5,000 km. The region from near the base of the diffusive layer to ~5,000 km in the lower transport region where the northern modulations are dominant corresponds to the region where the spacecraft was located above the photochemical equilibrium layer on field lines mapping inside the D ring. The region to ~7,000 km altitude beyond corresponds to field lines mapping from just inside the D ring to the central D ring region. Examination of the phases Δ_N in Figure 9c shows that in the region where the modulations are well-determined (not consistent with unity), phases Δ_N are close to zero in the diffusive layer, but fall to ‘earlier’ (negative) values typically by a few tens of degrees in the transport region.

Similar examination of the analysis results with respect to the southern PPO system in Figures 9e and 9f indicate the presence of relatively weak PPO modulations in the upper part of the diffusive layer above

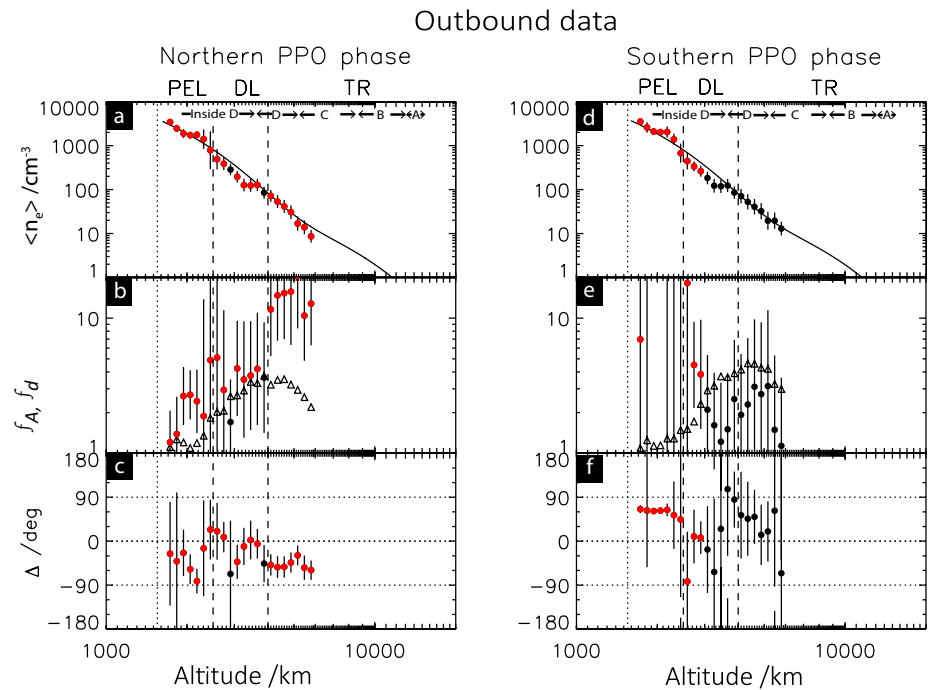


Figure 10. Overview of sinusoidal fit results for the southern hemisphere outbound electron density data in the same format as Figure 9.

~3,400 km, that are nevertheless inconsistent with unity within the uncertainties. The modulation factors are $f_{A_S} \sim 2$, comparable with the RMS deviation factors $f_{d_S} \sim 2$, again with near-zero phase Δ_S (see, e.g., Figure 6b). Modulation factors ~ 1.5 to ~ 2.5 are also found in the transport region from $\sim 5,000$ to $\sim 10,000$ km, also generally comparable with or a little larger than the RMS deviation factor f_{d_S} , again with somewhat ‘earlier’ phases by a few tens of degrees. These modulations span the inbound region of field lines mapping from inside Saturn’s D ring to the inner part of the C ring.

Figure 10 shows equivalent results for the southern hemisphere outbound data. We note from Figure 2 that to a first approximation the outbound data in the photochemical equilibrium layer below $\sim 2,500$ km correspond to sunlit conditions (as in Figure 8), the data in the transport region above $\sim 4,000$ km to shadow (as in Figure 7), while the data in the diffusive layer between these altitudes contain a variable mix of these conditions (as in Figure 6). Also as in Figure 6, to maximize phase coverage, all these data have been combined together irrespective. Figures 10a and 10d show that the mean electron density profiles are essentially the same within errors for the northern and southern PPO analyses as expected, and also similar to the corresponding Persoon et al. (2019) profile previously shown in Figure 3b (solid line). Due to the shadow effects, values fall more sharply with altitude (and latitude) than for the inbound data in Figures 9a and 9d, particularly above $\sim 4,000$ km in the transport region (Figure 3b and Persoon et al., 2019). Results for the northern PPO system modulation factor f_{A_N} in Figure 10b indicate the presence of factor ~ 3 – 4 modulations in the middle and upper diffusive layer (Figure 6c), though superposed on considerable additional data scatter with modestly smaller RMS deviation factors f_{d_N} . The modulations then increase in amplitude to become factor of ~ 10 in the transport region from $\sim 4,000$ to at least $\sim 6,000$ km (Figure 7c), compared with RMS deviation factors $f_{d_N} \approx 2 - 3$. Comparing with the ring region indicator in Figure 10a, significant northern system modulations were thus observed outbound over the whole region spanning D ring field lines, extending somewhat onto field lines inside the D ring on one side and onto C ring field lines on the other. As for the inbound data, phases Δ_N scatter about zero in the diffusive layer, but fall to ‘earlier’ (negative) values by a few tens of degrees in the transport region. However, evidence for significant southern system modulations in Figures 10e and 10f is much weaker than for the northern system, now with only an occasional altitude range, such as those in the inner diffusive layer, in which the southern PPO modulations are not consistent with unity.

4.4. Comparison With Magnetic Field Oscillations

We now compare the electron density modulation results in Figures 9 and 10 with the PPO-related magnetic field oscillations observed in the same region discussed briefly in Section 3.2. Provan, Cowley, Bradley, et al. (2019) have provided an extensive analysis of these oscillations similar in principle to that undertaken for the electron density data here, but where the pass-by-pass field data were organized by field line, specifically using the mapped ionospheric colatitude of the field lines as an appropriate coordinate, prior to sinusoid fitting. Here, as for the electron density in Section 4.1, we instead employ spacecraft altitude to organize the magnetic field data, so that a direct comparison can be made. Figure 2 shows, however, that these two approaches do not differ hugely in practice, since due to the grouped nature of the proximal pass trajectories, a given narrow band of altitudes on either the inbound or outbound passes generally corresponds to a relatively narrow band of planetary field lines. Thus we are able, for example, to indicate the approximate equatorial ring mapping of field lines at a given altitude inbound and outbound at the top of Figures 3a and 3b (also in Figures 9 and 10).

With regard to expectations, we recall from Section 4.3 (Figures 9 and 10) that the phase of the electron density modulations is such that the density maxima in the diffusive layer occur near the principal meridians of both PPO systems, $\Psi_{N,S} \approx 0^\circ$, moving to earlier phases by a few tens of degrees in the transport region. As indicated in Section 3.2, the principal meridians of both PPO systems are defined as the meridians in which the near-equatorial rotating quasi-uniform magnetic PPO perturbation field in the quasi-dipolar magnetosphere (outside the ring region) points directly radially outward. That is, to say, the density maxima are approximately in phase with the radial component of the perturbation field in this region, varying as $\sim \cos \Psi_{N,S}$ for the two systems. The density maxima are thus also approximately in leading quadrature with the azimuthal component of the perturbation field in this region varying as $\sim \sin \Psi_{N,S}$, while for the colatitudinal components they are in antiphase for the northern system varying as $\sim -\cos \Psi_N$ but in phase for the southern system varying as $\sim \cos \Psi_S$. However, using proximal pass data Provan, Cowley, Bradley, et al. (2019) showed that within the ring region, where the PPO oscillations are reasonably well-defined, the phase of each field component moves toward “earlier” phases by up to $\sim 90^\circ$, that is, $\Psi_{N,S} \rightarrow \Psi_{N,S} + 90^\circ$ in the above sinusoidal expressions. While the amplitude of the radial component oscillations on ring field lines is generally too small for the phases to be determined, the phasing of the azimuthal component thus moves from $\sim \sin \Psi_{N,S}$ to $\sim \cos \Psi_{N,S}$, while the phasing of the colatitudinal component moves from $\sim -\cos \Psi_N$ for the northern system and $\sim \cos \Psi_S$ for the southern system to $\sim \sin \Psi_N$ for the northern system and $\sim -\sin \Psi_S$ for the southern system. On this basis we expect the electron density to be modulated approximately in phase with the azimuthal field in the ring region for both systems, while being approximately in leading quadrature with the colatitudinal field perturbations for the northern system and in lagging quadrature for the southern system.

To make an accurate quantified assessment of these phase relations we now order the pass-by-pass field data into the same logarithmically spaced ranges of altitude as employed for the electron density data, and subject them to essentially the same sinusoid-fitting analysis. Similar to Provan, Cowley, Bradley, et al. (2019), we have employed 10 s averaged residual field data from which the Cao et al. (2020) planetary field has been subtracted, together with a ring current field determined from the Bunce et al. (2007) model for a typical subsolar magnetopause radius of $22 R_S$. Provan, Cowley, Bradley, et al. (2019) instead employed the Dougherty et al. (2018) planetary field together with the ring current field, but this makes no significant difference to these results. We note that the planetary field and the ring current field are both axisymmetric with zero azimuthal field, such that for the latter component the fields employed are those directly measured. Similar to the analysis of the electron density data in Section 4.1 (Equation 4), we least squares fit the following sinusoidal function to the residual data

$$B_{jN,S}(\Psi_{N,S}, h) = \langle B_{jN,S}(h) \rangle + A_{jN,S}(h) \cos(\Psi_{N,S} - \Delta_{jN,S}(h)), \quad (6)$$

where index $j = (r, \theta, \varphi)$ specifies the spherical polar field component referenced to the northern spin/magnetic axis of the planet. The fit parameters for a given field component are the mean residual field $\langle B_{jN,S} \rangle$, the oscillation amplitude $A_{jN,S}$, and the phase lag $\Delta_{jN,S}$. We note that since the maxima of the fitted sinusoid occur at phases $\Psi_{N,S} = \Delta_{jN,S}$ (modulo 360°), where $\Psi_{N,S}$ is a linearly increasing function of time at a given azimuth, values of $\Delta_{jN,S}$ lying in the range $0^\circ \leq \Delta_{jN,S} \leq 180^\circ$ (modulo 360°) correspond to “lagging” phases

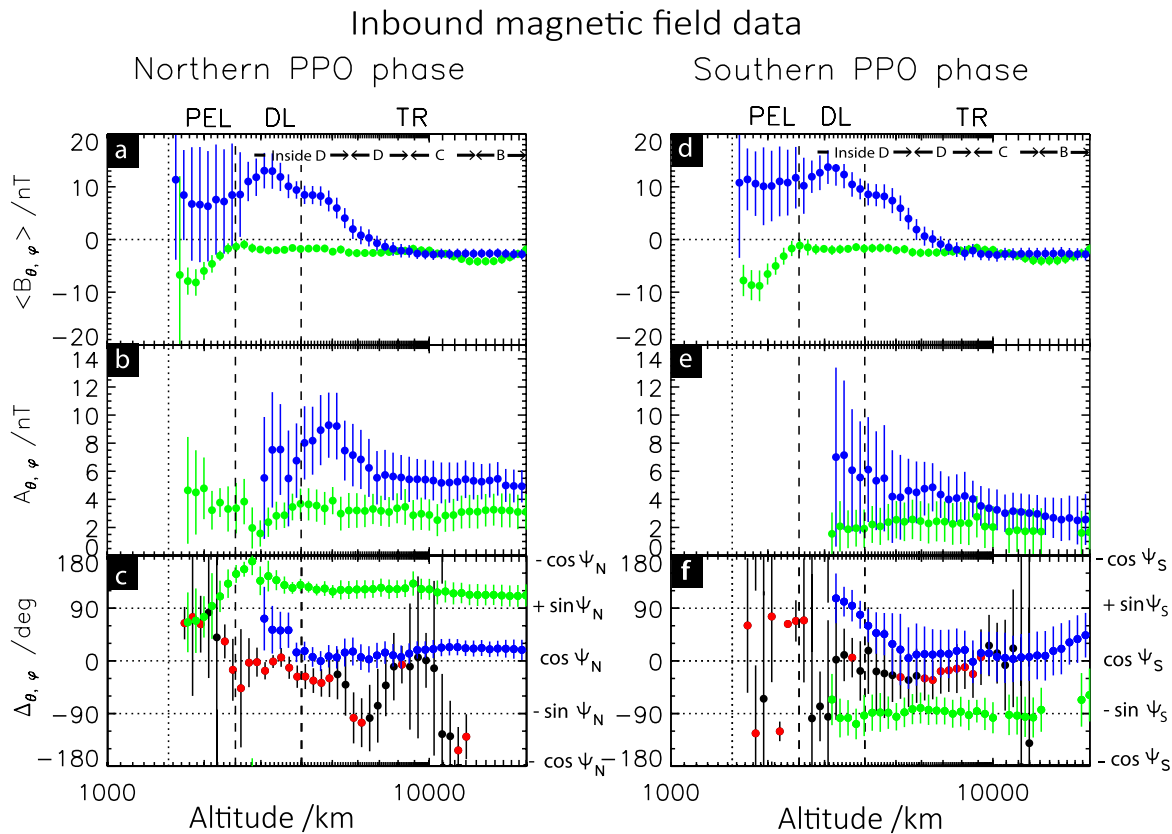


Figure 11. Sinusoidal fit results for the inbound pass magnetic field data in a similar format to Figure 9. The field data have been sorted into the same logged altitude ranges as for the electron density data (see further below), and least squares fitted to Equation 6 with respect to the northern planetary period oscillation (PPO) phases in panels (a–c), and with respect to the southern PPO phases in panels (d–f). Results for the azimuthal and colatitudinal components are shown in blue and green, respectively, while radial component results are omitted since these data produce essentially no amplitude/phase fits not consistent with zero in this regime. The logged altitude ranges employed for the colatitudinal component have been slipped by half a range bin compared with the azimuthal component to avoid overlapping and obscuring of the results. Mean values are shown for all altitude ranges having sufficient data in panels (a and d), respectively, while oscillation amplitudes and phases are shown in panels (b–e), and panel (f) only for fits where the amplitude is not consistent with zero within the estimated uncertainties. The red and black phase data in panels (c and d) on which the magnetic field phases are superposed show for purposes of comparison the corresponding phases of the electron density modulations reproduced from Figures 9c and 9f.

with a “later” maximum compared with $\cos\Psi_{N,S}$, while values of $\Delta_{j,N,S}$ lying in the range $-180^\circ \leq \Delta_{j,N,S} \leq 0^\circ$ (modulo 360°) correspond to “leading” phases with an “earlier” maximum compared with $\cos\Psi_{N,S}$.

Results for the field data from the inbound and outbound passes are shown in Figures 11 and 12, respectively, in a format similar to Figures 9 and 10 for the electron density data. Due to the essentially indeterminate nature of the radial component oscillations in this regime, only results for the azimuthal and colatitudinal field components are shown, indicated by blue and green data, respectively. The altitude ranges employed for the azimuthal component are identical to those for the electron density in Figures 9 and 10, but we have slipped the logged altitude by half a bin for the colatitudinal component so that the overlapping results for the two components do not obscure each other. Mean values are shown for all altitude ranges employed, while modulation parameters are shown only for fits where the oscillation amplitude is inconsistent with zero within the estimated uncertainties.

Examining the inbound mean field profiles in Figures 11a and 11d derived from the northern and southern PPO analyses, respectively, we note that these are essentially identical as expected. At lowest altitudes in the photochemical equilibrium and diffusive layers the azimuthal field is approximately constant at ~ 10 nT, falling to small near-constant negative values by $\sim 8,000$ km in the transport region. As indicated at the top of Figures 11a and 11d, the field lines in this region map into and inside of the D ring, such that this feature corresponds to the mean profile of the quasi-static azimuthal field perturbations previously discussed in

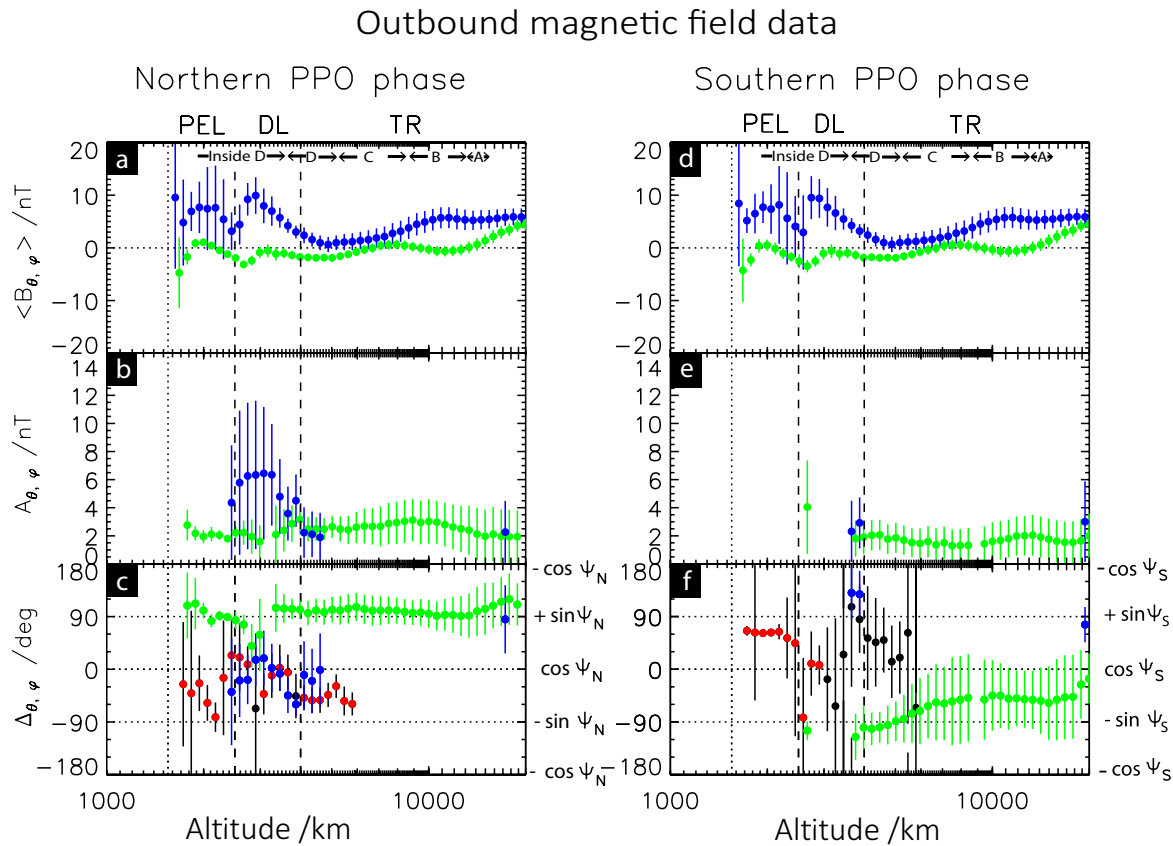


Figure 12. Sinusoidal fit results for the outbound pass magnetic field data in the same format as Figure 11. The electron density modulation phases shown red and black in panels (c and f) are reproduced from the electron density data in Figures 10c and 10f.

this region by, for example, Dougherty et al. (2018), Provan, Cowley, Bunce, et al. (2019), and Provan, Cowley, Bradley, et al. (2019). The colatitudinal component is near constant at small negative values throughout most of the altitude range, apart from a near-linear departure to larger negative values in the photochemical equilibrium layer.

The inbound oscillation amplitudes in Figures 11b and 11e indicate the presence of both northern and southern system oscillations in both the azimuthal and colatitudinal field components over much of the altitude range, similar to the previous results of Provan, Cowley, Bradley, et al. (2019) (see their Figures 10 and 11). Azimuthal component amplitudes are generally larger at smaller altitudes and gradually fall with increasing distance in the transport region, while colatitudinal component amplitudes are generally a factor ~ 2 smaller and more nearly constant with altitude. The amplitudes of both components are generally modestly larger for the northern system than for the southern system, again in line with the results of Provan, Cowley, Bradley, et al. (2019). We note that the inbound electron density data in Figures 9b and 9e also largely mirror these properties, showing dual modulation by both northern and southern PPO systems, with northern amplitudes that are usually larger than southern amplitudes.

Corresponding results for the oscillation phases are shown in Figures 11c and 11f for the northern and southern systems, respectively, where for purposes of comparison we have also shown the electron density modulation phases plotted in black and red, reproduced from Figures 9c and 9f. To a lowest approximation the ring region magnetic field phases are in line with those discussed above, with $\Delta_{\varphi_{N,S}} \approx 0^\circ$ such the northern and southern system azimuthal fields vary as $\sim \cos \psi_{N,S}$ similar to the electron density modulations, and with $\Delta_{\theta_N} \approx +90^\circ$ and $\Delta_{\theta_S} \approx -90^\circ$ such that the northern and southern colatitudinal fields vary as $\sim +\sin \psi_N$ and $\sim -\sin \psi_S$, respectively (as marked on the right hand sides of Figures 11c and 11f). At a more detailed level, however, it can be seen that the azimuthal field phases in the transport region are marginally later than $\Delta_{\varphi_{N,S}} = 0^\circ$ by $\sim 10^\circ - 20^\circ$, moving to somewhat larger values in the diffusive layer, while the electron

density phases are typically a little earlier in the transport region as indicated in Section 4.3. The net result is that where both phases are well-determined, the maxima in the azimuthal field component occur $\sim 30^\circ$ – 50° later than those of the electron density, corresponding to approximately one ninth of a full cycle. In addition, for the northern system in Figure 11c, the colatitudinal field phases are typically $\sim 100^\circ$ – 120° later than those of the azimuthal component, rather than the expected $\sim 90^\circ$, such that the maxima in the colatitudinal component occur $\sim 140^\circ$ – 160° later than those of the electron density, nearer to antiphase than to lagging quadrature. For the southern system in Figure 11f, the colatitudinal field maxima occur $\sim 100^\circ$ – 110° earlier than those of the azimuthal component (close to $\Delta\theta_S \approx -90^\circ$), and hence $\sim 50^\circ$ – 70° earlier than those of the electron density, a phase difference that is, $\sim 20^\circ$ – 40° less than that of leading quadrature.

Corresponding results for the outbound pass data are shown in Figure 12. In Figures 12a and 12d the large positive values of the mean azimuthal component again correspond to field lines mapping into and inside the D ring, now extending only to altitudes $\sim 5,000$ km just above the diffusive layer, rather than to $\sim 8,000$ km in the transport region as in the inbound data in Figures 11a and 11d. These results are thus consistent with the expectation that this quasi-static azimuthal field feature is organized by field line rather than by altitude. Above this region the mean outbound azimuthal field then exhibits smaller but again growing positive values rather than small negative values as in the inbound data, in line with the previous results of Provan, Cowley, Bradley, et al. (2019) (their Figure 18c).

In Figures 12b and 12e, oscillations with amplitudes not consistent with zero within the uncertainties are generally found only in the colatitudinal component, extending over much of the altitude range for both systems, though northern system azimuthal component oscillations with large uncertainties are detected in the outbound diffusive layer. Amplitudes are again somewhat less for the southern system than for the northern, and overall are also somewhat less than for the inbound data in Figures 11b and 11e for both systems, again similar to the results of Provan, Cowley, Bradley, et al. (2019) (their Figures 10 and 11). These trends are again similar to those found in the electron density data in Figures 9 and 10, in that the weakest evidence for PPO-related oscillations occurs for the southern system in the outbound data. The outbound magnetic field phase data in Figures 12c and 12f are similar to those for the inbound data in Figures 11c and 11f within the uncertainties, though rather more scattered for the few azimuthal component determinations for the northern system in Figure 12c. To the extent that they can be determined, essentially only for the northern system modulations, the phase differences with the outbound electron density data are consistent with those more reliably determined from the inbound data.

Figures 13a and 13b show simple sketches which summarize the empirical phase relationships between the electron density and magnetic field modulations for the northern and southern PPO systems, respectively. For reasons indicated above these are based principally on the inbound results in Figures 11c and 11f, respectively. In both diagrams the view is from the north looking down onto the equatorial region, where the orange circle represents the body of the planet. Within this area we indicate the orientation of the local phases of the PPO systems, $\Psi_{N,S}$, where the principal meridians ($\Psi_{N,S} = 0^\circ$) are taken to lie at the bottom of the diagrams in each case. The exterior purple region schematically indicates the topside ionosphere, where a contour of given electron density shown by the purple dashed line rises and falls in altitude with the PPO phase resulting in periodic density modulations as the PPO system rotates. The phases of maximum and minimum density at a given altitude are indicated by the inclined black dashed line, marked $+n_e$ at the maximum and $-n_e$ at the minimum. The phases illustrated correspond to the lower transport region $\sim 4,000$ – $5,000$ km altitude where the phases of the electron density and magnetic field oscillations for both systems are reasonably well determined, with the phase of maximum density being a few tens of degrees “earlier” than that of the principal meridians (by $\sim 30^\circ$ for the northern system in Figure 13a and by $\sim 25^\circ$ for the southern system in Figure 13b). In the diffusive layer at lower altitudes $\sim 3,000$ km the $+n_e$ phase moves toward the principal meridian for both systems. The magnetic field symbols within the ionospheric region show the PPO phases at which the relevant component has its maximum (+symbol) and minimum (– symbol) values, where the blue arrows indicate the azimuthal component (B_ϕ), and the green circled symbols indicate the colatitudinal component (B_θ). Circled crosses indicate vectors pointed into the plane of the diagram (positive B_θ), while circled dots indicate vectors pointed out of the plane of the diagram (negative B_θ). The related black magnetic field symbols in the outer part of the diagram indicate the phases of the component maxima and minima at larger distances in the equatorial region, outside of the ring region,

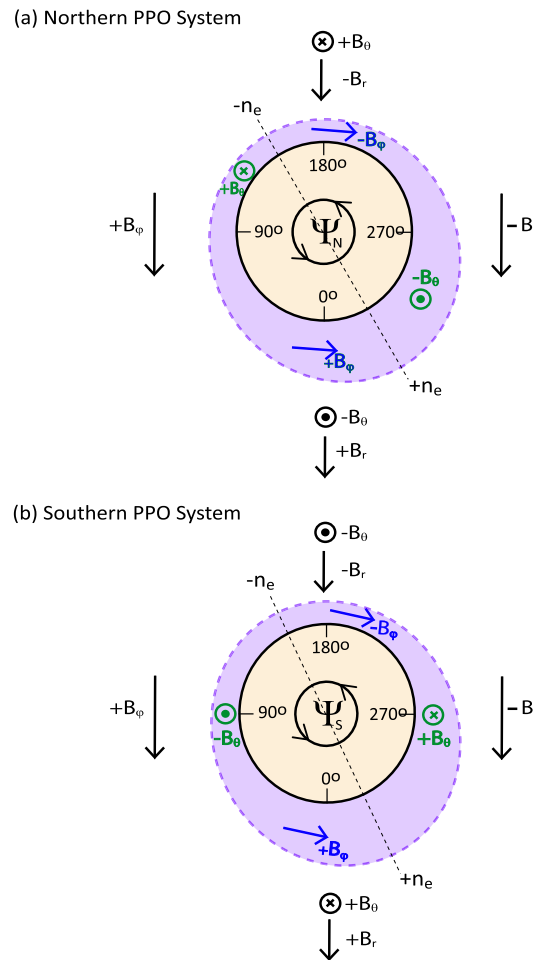


Figure 13. Sketches summarizing the empirical phase relationships of the near-equatorial ionospheric electron density and magnetic field oscillations for (a) the northern planetary period oscillation (PPO) system and (b) the southern PPO system, based principally on the inbound phase results shown in Figures 11c and 11f. The view in each diagram is from the north looking down onto the equatorial region. The orange circle represents the body of the planet, wherein we indicate the orientation of the local phases of the PPO systems, $\Psi_{N,S}$, with the principal meridians $\Psi_{N,S} = 0^\circ$ located at the bottom in each case. The purple region outside schematically indicates the topside ionosphere, with a given contour of electron density indicated by the purple dashed line rising and falling with PPO phase giving rise to periodic density maxima and minima at a fixed altitude as the system rotates anticlockwise with the corresponding PPO period. The phase meridians of maximum and minimum density are indicated by the inclined black dashed line, marked $+n_e$ for the maximum and $-n_e$ for the minimum. For definiteness, the phases illustrated correspond to the lower transport region $\sim 4,000\text{--}5,000$ km altitude where the phases of both density and magnetic field oscillations for both systems are reasonably well determined. Magnetic field symbols within the ionospheric region indicate the PPO phases at which the component concerned has its maximum (+) and minimum (–), where the blue arrows indicate the azimuthal component (B_ϕ), and the green circled symbols indicate the colatitudinal component (B_θ). Circled dots and crosses indicate vectors pointed out of and into the plane of the diagram, respectively. The black magnetic field symbols indicate the phases of the corresponding component maxima and minima at larger near-equatorial radial distances outside of the ring region, including the radial component oscillations that could not be reliably determined within the ring region itself.

including the radial component oscillations that could not be reliably determined within the ring region itself. The rotation of the magnetic field oscillation phases in the inner region to “earlier” values by $\sim 90^\circ$ compared with the outer region is evident. With increasing time, this pattern of density and field perturbations rotates anticlockwise as indicated, with the corresponding PPO period.

5. Summary and Discussion

In this study we have examined the electron density data acquired in Saturn's near-noon equatorial ionosphere during the final 23 proximal orbits of the Cassini spacecraft in 2017, specifically the values deduced by Persoon et al. (2019) from analysis of electric field wave spectra. Provan, Cowley, Bradley, et al. (2019) have shown that the magnetic field modulations (PPOs) that rotate near the planetary period throughout the magnetosphere are also present on these orbits on field lines passing through Saturn's equatorial ring system to near-equatorial periapsis. Here we have therefore examined whether such modulations are also present in the ionospheric electron density data in the same region.

By examining the pass-by-pass variations in density under conditions of differing PPO phase, we have shown that density modulations are indeed present, in general simultaneously with respect to both the northern and southern PPO systems. Clear evidence for northern system modulations has been found in the ionospheric diffusive layer on the northern hemisphere and equatorial region inbound passes, peaking at a modulation factor of ~ 7 at $\sim 3,200$ km altitude, then falling to a factor of ~ 4 at $\sim 5,000$ km in the transport region, and to values below ~ 2 consistent within uncertainties to unity (no effect) by $\sim 7,000$ km. On the inbound passes, this region spans field lines from those mapping inside the D ring to the central region of the D ring. The modulation factors in the diffusive layer and lower transport region are larger than the factors associated with the RMS deviation of the data about the modulated fit values, typically a factor ~ 2 , so that the PPO system contributes significantly to the variability of the electron density data in this region. Weaker simultaneous southern system modulations by factors of ~ 1.5 – ~ 2.5 were also detected in the upper part of the diffusive layer above $\sim 3,400$ km, and between $\sim 5,000$ and $\sim 10,000$ km in the transport region, now corresponding to field lines spanning from inside the D ring to the inner part of the C ring. These modulations are generally comparable with or a little larger than the factor of ~ 2 modulations associated with the RMS deviation of the data. No evidence of significant PPO modulations were found in the lower altitude photochemical equilibrium layer of highest densities at altitudes $\sim 1,600$ – $2,200$ km.

Northern system modulations were also observed in the southern hemisphere outbound pass data, by factors of ~ 3 – 4 in the diffusive layer above $\sim 3,000$ km altitude, jumping to factors of ~ 10 in the transport region above $\sim 4,000$ km to at least $\sim 6,000$ km. On the outbound passes this altitude regime corresponds to field lines mapping from just inside the inner edge of the D ring to just outside the inner edge of the C ring. The modulation factors associated with the RMS deviations are ~ 2 – 3 in this region. However, with the possible exception of a region in the lower diffusive layer, no evidence for southern system modulations could be discerned within the overall variability of the data on the outbound passes.

In essentially all cases where clear electron density modulations were observed, their phases relative to the northern Ψ_N and southern Ψ_S magnetic field PPO phases of Provan et al. (2018) were near zero in the diffusive layer, that is, varying as $\sim \cos \Psi_{N,S}$, moving to somewhat 'earlier' phases by a few tens of degrees, that is, with a smaller additional $-\sin \Psi_{N,S}$ component, in the transport region above. The PPO phases for the proximal pass interval were empirically determined by Provan et al. (2018) from magnetic field data obtained around apoapsis on the nightside of the planet. The density modulations are thus approximately in phase with the radial perturbation fields in the near-equatorial quasi-dipolar magnetosphere outside of the ring region for both systems, both varying as $\sim \cos \Psi_{N,S}$ (Figure 13). They are therefore also in leading quadrature with the azimuthal perturbation fields in this region varying as $\sim \sin \Psi_{N,S}$, while being in phase with the colatitudinal perturbation field for the southern system varying as $\sim \cos \Psi_S$, but in antiphase with the colatitudinal perturbation field for the northern system varying as $\sim -\cos \Psi_N$. Previously, however, Provan, Cowley, Bradley, et al. (2019) have shown that the magnetic oscillations on ring region field lines have altered phases with respect to those observed at larger distances in the quasi-dipolar magnetosphere outside the ring region, to a first approximation moving toward "earlier" phases by $\sim 90^\circ$. In this case the azimuthal perturbation fields vary as $\sim \cos \Psi_{N,S}$, approximately in phase with the density modulations, while the colatitudinal perturbation fields vary as $\sim \sin \Psi_N$ and $\sim -\sin \Psi_S$ for the two systems, with the density variations then being in approximate leading and lagging quadrature, respectively.

We have therefore directly examined the phase relationships between the electron density modulations and the magnetic field oscillations on the proximal passes using pass-by-pass magnetic field analyses organized similarly by altitude. The results first show related behavior in the two data sets, with higher amplitude

magnetic field oscillations observed inbound than outbound for both PPO systems, together with somewhat stronger northern than southern system oscillations in both regimes. With regard to the phases, detailed examination shows that the maxima in the electron density occur $\sim 30^\circ$ – 50° earlier than those of the azimuthal field component for both systems, corresponding to approximately one ninth of a full cycle. To the extent that these modulations may be regarded as being reasonably closely in phase, this implies that enhanced electron densities occur when the azimuthal field is positive such that the total field tilts slightly anticlockwise from southward as viewed from the Sun, while reduced electron densities occur when the azimuthal field is negative such that the total field tilts slightly clockwise as viewed from the Sun. Related radial component oscillations are too small to analyze. We also find that for the northern system, the electron density maxima occur $\sim 140^\circ$ – 160° earlier than those of the colatitudinal field, nearer to antiphase than to leading quadrature, while for the southern system the electron density maxima occur $\sim 50^\circ$ – 70° later than those of the colatitudinal field thus somewhat less than that of lagging quadrature. These results were determined principally from the northern and equatorial inbound pass data. Results from the southern outbound pass data are more scattered, but consistent to the extent that they can be determined.

While this study has concentrated on establishing the empirical facts concerning PPO modulations of Saturn's ionospheric electron density, the topic of the physical mechanism has yet to be addressed and remains for future consideration. One possible Saturn-specific mechanism relates to modulation of the 'ring rain' dust influx into the low-latitude ionosphere from Saturn's rings (e.g., Hsu et al., 2018; Mitchell et al., 2018; Moore et al., 2018; O'Donoghue et al., 2013, 2017; Perry et al., 2018; Waite et al., 2018), it being known that the PPO perturbations that pervade the ring region can indeed affect tenuous ring material (Chancia et al., 2019; Hedman et al., 2009; Mitchell et al., 2013; Porco & Danielson, 1982). A more direct possibility relates to the effect of the twin-vortex atmospheric/ionospheric flows originating in the two polar regions that drive the magnetosphere-wide northern and southern PPO modulations (e.g., Bradley et al., 2018). The effect of these flow systems clearly extends across the planetary equator, conceivably modulating the uplift of the equatorial ionosphere via the "fountain" effect associated with the azimuthal electric field, analogous to the effect of magnetic storm intervals on the Earth's equatorial ionosphere (e.g., Kelley et al., 2010; Tsurutani et al., 2004). Examination shows, however, that the azimuthal electric fields at given values of the local phase $\Psi_{N,S}$ are directed oppositely for the two PPO systems, while our results show the electron density modulations depend similarly on the local phase, for example, with maxima where $\Psi_{N,S} \approx 0^\circ$. The same anti-symmetry is true of the azimuthal atmospheric winds, while the meridional winds are similarly directed for the two systems, both flowing from north to south at local phases centered on $\Psi_{N,S} = 0^\circ$, and from south to north at local phases centered on $\Psi_{N,S} = 180^\circ$. Meridional winds are known to play an important role in the equatorial ionosphere at Earth, with ion-neutral collisions resulting in both vertical plasma transport along inclined field lines, as well potentially as hemispheric transport across the equator (e.g., Khadka et al., 2018). At Saturn, we might then envisage strong upward and trans-equatorial transport of plasma from the northern summer ionosphere to the southern winter ring-shadowed ionosphere when the wind is directed from north to south centered on $\Psi_{N,S} = 0^\circ$, with weaker effects occurring in the opposite direction when the wind is directed from south to north centered on $\Psi_{N,S} = 180^\circ$, possibly leading to the density modulations observed. We also note that the PPO-related neutral atmospheric wind systems likely rotate with the body of the mid- and low-latitude atmosphere to within $\sim 1\%$, so that even with expected modest meridional wind speeds of order $\sim 0.1 \text{ km s}^{-1}$, significant transport may occur given winds that persist in direction over many Saturn days. Whatever the mechanism, however, we finally emphasize that the effect on the equatorial topside ionosphere is not a small one, involving density variations corresponding to factors of up to ~ 2 ionospheric scale heights.

Data Availability Statement

The electron density data employed here are available at the NASA Planetary Data System at https://pds.nasa.gov/ds-view/pds/viewCollection.jsp?identifier=urn:nasa:pds:cassini-rpws-electron_density:data-&version=1.0. PPO phase data (2004–2017) are available from the University of Leicester Research Archive (<http://hdl.handle.net/2381/42436>).

Acknowledgments

Work at the University of Leicester was supported by STFC grant ST/N000749/1. Research at the University of Iowa was supported by NASA through contract 1415150 with the Jet Propulsion Laboratory, and by the University of Iowa. E. J. Bunce was supported by a Royal Society Wolfson Research Merit Award. The authors would like to thank Gregory Hunt, Aurélie Marchaudon, Luke Moore, and Timothy Yeoman for helpful discussions on physical mechanisms.

References

- Agiwal, O., Cao, H., Cowley, S. W. H., Dougherty, M. K., Hunt, G. J., Müller-Wodarg, I., & Achilleos, N. (2021). Constraining the temporal variability of neutral winds in Saturn's low-latitude ionosphere using magnetic field measurements. *Journal of Geophysical Research: Planets*, *126*, e2020JE006578. <https://doi.org/10.1002/2020JE006578>
- Bradley, T. J., Cowley, S. W. H., Provan, G., Hunt, G. J., Bunce, E. J., Wharton, S. J., et al. (2018). Field-aligned currents in Saturn's nightside magnetosphere: Subcorotation and planetary period oscillation components during northern spring. *Journal of Geophysical Research: Space Physics*, *123*, 3602–3636. <https://doi.org/10.1002/2017JA024885>
- Bunce, E. J., Cowley, S. W. H., Alexeev, I. I., Arridge, C. S., Dougherty, M. K., Nichols, J. D., & Russell, C. T. (2007). Cassini observations of the variation of Saturn's ring current parameters with system size. *Journal of Geophysical Research*, *112*, A10202. <https://doi.org/10.1029/2007JA012275>
- Cao, H., Dougherty, M. K., Hunt, G. J., Provan, G., Cowley, S. W. H., Bunce, E. J., et al. (2020). The landscape of Saturn's internal magnetic field from the Cassini grand finale. *Icarus*, *344*, 113541. <https://doi.org/10.1016/j.icarus.2019.113541>
- Chancia, R. O., Hedman, M. M., Cowley, S. W. H., Provan, G., & Ye, S.-Y. (2019). Seasonal structures in Saturn's dusty Roche division are tied to periodicities in the planet's magnetosphere. *Icarus*, *330*, 230–255. <https://doi.org/10.1016/j.icarus.2019.04.012>
- Connerney, J. E. P., & Waite, J. H. (1984). New model of Saturn's ionosphere with an influx of water from the rings. *Nature*, *312*, 136–138. <https://doi.org/10.1038/312136a0>
- Dougherty, M. K., Cao, H., Khurana, K. K., Hunt, G. J., Provan, G., Kellock, S., et al. (2018). Saturn's magnetic field revealed by Cassini's grand finale. *Science*, *362*, eaat5434. <https://doi.org/10.1126/science.aat5434>
- Farrell, W. M., Hadid, L. Z., Morooka, M. W., Kurth, W. S., Wahlund, J.-E., MacDowall, R. J., et al. (2018). Saturn's plasma density depletions along magnetic field lines connected to the main rings. *Geophysical Research Letters*, *45*, 8104–8110. <https://doi.org/10.1029/2018GL078137>
- Fischer, G., Gurnett, D. A., Zarka, P., Moore, L., & Dyudina, U. A. (2011). Peak electron densities in Saturn's ionosphere derived from the low-frequency cut-off of Saturn lightning. *Journal of Geophysical Research*, *116*, A045315. <https://doi.org/10.1029/2010JA016187>
- Gurnett, D. A., Kurth, W. S., Kirchner, D. L., Hospodarsky, G. B., Averkamp, T. F., Zarka, P., et al. (2004). The Cassini radio and plasma wave investigation. *Space Science Reviews*, *114*, 395–463. <https://doi.org/10.1007/s11214-004-1434-0>
- Hadid, L. Z., Morooka, M. W., Wahlund, J.-E., Moore, L., Cravens, T. E., Hedman, M. M., et al. (2018). Ring shadowing effects on Saturn's ionosphere: Implications for ring opacity and plasma transport. *Geophysical Research Letters*, *45*, 10084–10092. <https://doi.org/10.1029/2018GL079150>
- Hadid, L. Z., Morooka, M. W., Wahlund, J.-E., Persoon, A. M., Andrews, D. J., Shebanits, O., et al. (2019). Saturn's ionosphere: Electron density altitude profiles and D ring interaction from the Cassini grand finale. *Geophysical Research Letters*, *46*, 9362–9369. <https://doi.org/10.1029/2018GL078004>
- Hamil, O., Cravens, T. E., Reedy, N. L., & Sakai, S. (2018). Fate of ice grains in Saturn's ionosphere. *Journal of Geophysical Research: Space Physics*, *123*, 1429–1440. <https://doi.org/10.1002/2017JA024616>
- Hedman, M. M., Burns, J. A., Tiscareno, M. S., & Porco, C. C. (2009). Organizing some very tenuous things: Resonant structures in Saturn's faint rings. *Icarus*, *202*, 260–279. <https://doi.org/10.1016/j.icarus.2009.02.016>
- Hsu, H.-W., Schmidt, J., Kempf, S., Postberg, F., Moragas-Klostermayer, G., Seiss, M., et al. (2018). In situ collection of dust grains falling from Saturn's rings into its atmosphere. *Science*, *362*, eaat3185. <https://doi.org/10.1126/science.aat3185>
- Kelley, M. C., Ilma, R. R., Nicolls, M., Erickson, P., Goncharenko, L., Chau, J. L., et al. (2010). Spectacular low- and mid-latitude electric fields and neutral winds during a superstorm. *Journal of Atmospheric and Solar-Terrestrial Physics*, *72*, 285–291. <https://doi.org/10.1016/j.jastp.2008.12.006>
- Khadka, S. M., Valladares, C. E., Sheehan, R., & Gerrard, A. J. (2018). Effects of electric field and neutral wind on the asymmetry of equatorial ionization anomaly. *Radio Science*, *53*, 683–697. <https://doi.org/10.1029/2017RS006428>
- Khurana, K. K., Dougherty, M. K., Provan, G., Hunt, G. J., Kivelson, M. G., Cowley, S. W. H., et al. (2018). Discovery of atmospheric-wind-driven electric currents in Saturn's magnetosphere in the gap between Saturn and its rings. *Geophysical Research Letters*, *45*, 10068–10074. <https://doi.org/10.1002/2018GL078256>
- Kliore, A. J., Nagy, A., Asmar, S., Anabtawi, A., Barbinis, E., Fleischman, D., et al. (2014). The ionosphere of Saturn as observed by the Cassini radio science system. *Geophysical Research Letters*, *41*, 5778–5782. <https://doi.org/10.1002/2014GL060512>
- Mitchell, C. J., Porco, C. C., Dones, H. L., & Spitale, J. N. (2013). The behavior of spokes in Saturn's B ring. *Icarus*, *225*, 446–474. <https://doi.org/10.1016/j.icarus.2013.02.011>
- Mitchell, D. G., Perry, M. E., Hamilton, D. C., Westlake, J. H., Kollmann, P., Smith, H. T., et al. (2018). Dust grains fall from Saturn's D-ring into its equatorial upper atmosphere. *Science*, *362*, eaat2236. <https://doi.org/10.1126/science.aat2236>
- Moore, L., Cravens, T. E., Müller-Wodarg, I., Galand, M., Perry, M. E., Waite, J. H., Jr, et al. (2018). Models of Saturn's equatorial ionosphere based on in situ data from Cassini's grand finale. *Geophysical Research Letters*, *45*, 9398–9407. <https://doi.org/10.1029/2018GL078162>
- Morooka, M. W., Wahlund, J.-E., Hadid, L. Z., Eriksson, A. I., Edberg, N. J. T., Vigren, E., et al. (2019). Saturn's dusty ionosphere. *Journal of Geophysical Research: Space Physics*, *124*, 1679–1697. <https://doi.org/10.1002/2018JA026154>
- O'Donoghue, J., Moore, L., Connerney, J. E. P., Melin, H., Stallard, T. S., Miller, S., & Baines, K. H. (2017). Redetection of the ionospheric H₃⁺ signature of Saturn's 'ring rain'. *Geophysical Research Letters*, *44*, 11762–11769. <https://doi.org/10.1002/2017GL075932>
- O'Donoghue, J., Stallard, T. S., Melin, H., Jones, G. H., Cowley, S. W. H., Miller, S., et al. (2013). The domination of Saturn's low latitude ionosphere by ring 'rain'. *Nature*, *496*, 193–195. <https://doi.org/10.1038/nature12049>
- Perry, M. E., Waite, J. H., Jr, Mitchell, D. G., Miller, K. E., Cravens, T. E., Perryman, R., et al. (2018). Material flux from the rings of Saturn into its atmosphere. *Geophysical Research Letters*, *45*, 10093–10100. <https://doi.org/10.1029/2018GL078575>
- Persoon, A. M., Kurth, W. S., Gurnett, D. A., Groene, J. B., Sulaiman, A. H., Wahlund, J.-E., et al. (2019). Electron density distributions in Saturn's ionosphere. *Geophysical Research Letters*, *46*, 3061–3068. <https://doi.org/10.1029/2018GL078020>
- Porco, C. C., & Danielson, G. E. (1982). The periodic variation of spokes in Saturn's rings. *The Astronomical Journal*, *87*, 826–833.
- Provan, G., Cowley, S. W. H., Bradley, T. J., Bunce, E. J., Hunt, G. J., Cao, H., & Dougherty, M. K. (2019). Magnetic field observations on Cassini's proximal periapsis passes: Planetary period oscillations and mean residual fields. *Journal of Geophysical Research: Space Physics*, *124*, 8814–8864. <https://doi.org/10.1002/2019JA026800>
- Provan, G., Cowley, S. W. H., Bradley, T. J., Bunce, E. J., Hunt, G. J., & Dougherty, M. K. (2018). Planetary period oscillations in Saturn's magnetosphere: Cassini magnetic field observations over the northern summer solstice interval. *Journal of Geophysical Research: Space Physics*, *123*, 3859–3899. <https://doi.org/10.1002/2018JA025237>

- Provan, G., Cowley, S. W. H., Bunce, E. J., Bradley, T. J., Hunt, G. J., Cao, H., & Dougherty, M. K. (2019). Variability of intra-D ring azimuthal magnetic field profiles observed on Cassini's proximal periapsis passes. *Journal of Geophysical Research: Space Physics*, *124*, 379–404. <https://doi.org/10.1002/2018JA026121>
- Shebanits, O., Hadid, L. Z., Cao, H., Morooka, M. W., Hunt, G. J., Dougherty, M. K., et al. (2020). Saturn's near-equatorial ionospheric conductivities from in situ measurements. *Scientific Reports*, *10*, 7932. <https://doi.org/10.1038/s41598-020-64787-7>
- Tsurutani, B., Mannuchi, A., Iijima, B., Abdu, M. A., Sobral, J. H. A., Gonzalez, W., et al. (2004). Global dayside ionospheric uplift and enhancement associated with interplanetary electric fields. *Journal of Geophysical Research*, *109*, A08302. <https://doi.org/10.1029/2003JA010342>
- Wahlund, J.-E., Morooka, M. W., Hadid, L. Z., Persoon, A. M., Farrell, W. M., Gurnett, D. A., et al. (2018). In situ measurements of Saturn's ionosphere show that it is dynamic and interacts with the rings. *Science*, *359*, 66–68. <https://doi.org/10.1126/science.aao4134>
- Waite, J. H., Jr, Perryman, R. S., Perry, M. E., Miller, K. E., Bell, J., Cravens, T. E., et al. (2018). Chemical interactions between Saturn's atmosphere and its rings. *Science*, *362*, eaat2383. <https://doi.org/10.1126/science.aat2382>
- Xin, L., Gurnett, D. A., Santolik, O., Kurth, W. S., & Hospodarsky, G. B. (2006). Whistler mode auroral hiss emissions observed near Saturn's B ring. *Journal of Geophysical Research*, *111*, A06214. <https://doi.org/10.1029/2005JA011432>
- Ye, S.-Y., Kurth, W. S., Hospodarsky, G. B., Persoon, A. M., Sulaiman, A. H., Gurnett, D. A., et al. (2018). Dust observations by the radio and plasma wave science instrument during Cassini's grand finale. *Geophysical Research Letters*, *45*, 10101–10109. <https://doi.org/10.1029/2018GL078059>